Provision of Top-Of-Atmosphere simulations for the MAP and CLIM instruments of the CO2 monitoring mission

V 2.0

HYGEOS

Laboratoire d'Optique Atmosphérique

ICARE service and data center

Project Team

Document change record

- Version 1 delivered on 09/09/2023
- Version 2 delivered on 24/11/2023 following comments from EUMETSAT and test data users
- Version 3 describe the test data v2

Document Distribution

Document Editor

Mathieu Compiègne, HYGEOS

Visa:

Document Reference

HYGEOS/MAP-CLIM-SDS-Follow-on/FinalReport

1. Contents

2. Introduction to the v2 test data production

This report is an update of the previous version describing a new production of test data (v2) with modifications with respect to v1 test data. Modifications concern both the instrument design and the scene description. For the scene description, the same modifications were applied to the production of the CO2IS test data. For v2 test data, no hyperspectral data were produced.

The instrument design modifications were applied by EUMETSAT and provided to us through the production of new L1 footprint and lines of sight. Among changes applied, we can notice

- the inversion of CLIM 3A and C lines of sight
- update of the CLIM spectral response function
- individual footprint for each MAP channel

The changes to the scene description are the following:

- Land / water fraction accounted for at pixel level for MAP and CLIM (note however that for CLIM, LSM is not fractional but in v1 it was only varied at “super pixel” scale)
- Sea ice fraction accounted for at pixel level (for MAP and CLIM)
- Snow depth ancillary data not used anymore
- For BRDF parameters, the 753 nm channels are forced to the 858.5 nm wavelength

Beside those changes, a couple of problem with v1 test data were corrected in the present version:

- Correction of the “organic matter issue”:
    - In v1 test data, OMAOD550 was omitted in normalizing the Sulphate + organic matter aerosol profile. The shape of the profile was computed accounted for both sulphate and organic matter but it was normalized only accounting for suaod550. In section 9.1 equation $\sigma_{ext550,SUOM}(z) = \sigma_{ext,SUOM}(z)\frac{AOD_{SU550}}{\int \sigma_{ext,SUOM}(z)\,dz}$ should have been $\sigma_{ext550,SUOM}(z) = \sigma_{ext,SUOM}(z)\frac{AOD_{SU550}+AOD_{OM550}}{\int \sigma_{ext,SUOM}(z)\,dz}$. The total AOD550 in our scene is BCAOD550+SSAOD550+SUAOD550+DUAOD550
- Correction of the weighting of incoming solar flux and SIF computation as averaged into SRFs

In v2 test data, the sign of U Stokes parameter follows the same convention as Polder/Parasol and 3MI data. It corresponds to -U regarding v1 test data.

3. Purpose and scope of the study

The present report describes results of a study aiming at producing synthetic top-of-atmosphere test data for the Multi-Angle Polarimeter (MAP) and Cloud Imager (CLIM) instrument of the CO2M mission. The test data will essentially be used for testing of the CO2M Payload Data Processing Segment (PDPS).

Key elements of the work were to provide full-orbit test datasets for MAP and CLIM observations consistent with the design and purpose of the CO2M platform and supporting the simulation of cloud and aerosol retrievals from the test-data. The latter are in turn supporting the retrieval of greenhouse-gas products, as well as nitrogen oxide from the main spectrometer instrument on-board CO2M. Test-data generated for the main CO2M spectrometer are provided through a separate study (RAL, 2021).

The overall objectives of the study were the following:

1. The provision of simulated top-of-atmosphere (ToA) polarised radiance data for MAP and CLIM, based on observation geometries of six CO2M orbits for both instruments. Observation geometries including parallax corrected geolocation calculation using terrain-height data were provided by EUMETSAT. Instrument specific design aspects like ISRF, spectral resolution and other relevant instrument performance figures were taken from the SSRD requirements document. Atmospheric and surface modelling fields and other ancillary data were provided through the dedicated test-data study for the main spectrometer instrument on CO2M. This is to ensure maximum consistency of observation geometries and model atmosphere between all CO2M instrument test datasets. The provided atmospheric modelling fields were only complemented by additional modelling or model parameters in case absolutely required for realistic modelling of MAP and CLIM observations (e.g. related to polarisation modelling).
2. Establishing a ToA polarised radiance simulation framework for the MAP and CLIM instrument, which can be re-used for subsequent (revised) ToA test-data simulations by adopting different instrument settings, or testing various (instrument) performance scenarios, or expanding on the number of orbits and satellite platforms simulated.

The study was performed based on our previous experience and heritage tools to produce TOA synthetic radiance gained through two EUMETSAT studies:

- “EPS Second Generation – Test data for the METimage and 3MI instruments” to produce 3MI and METimage instrument being instruments producing measurements with characteristics close to the MAP and CLIM one.
- “High Spectral Resolution synthetic radiance for Geostationary imagers” to produce high spectral resolution radiance, for a hypothetical instrument, with characteristics close to the requirement in terms of spectral over-sampling for the present study.

The produced test data corresponds to MAP and CLIM L1B radiance with the nominal spectral resolution. MAP test data directly in the L1C pixel grid and geometries were also produced. That will be used for the assessment of error related to the pixel collocation going from L1B to L1C grid.

This work was committed by EUMETSAT and funded by Copernicus.

4. Input from EUMETSAT

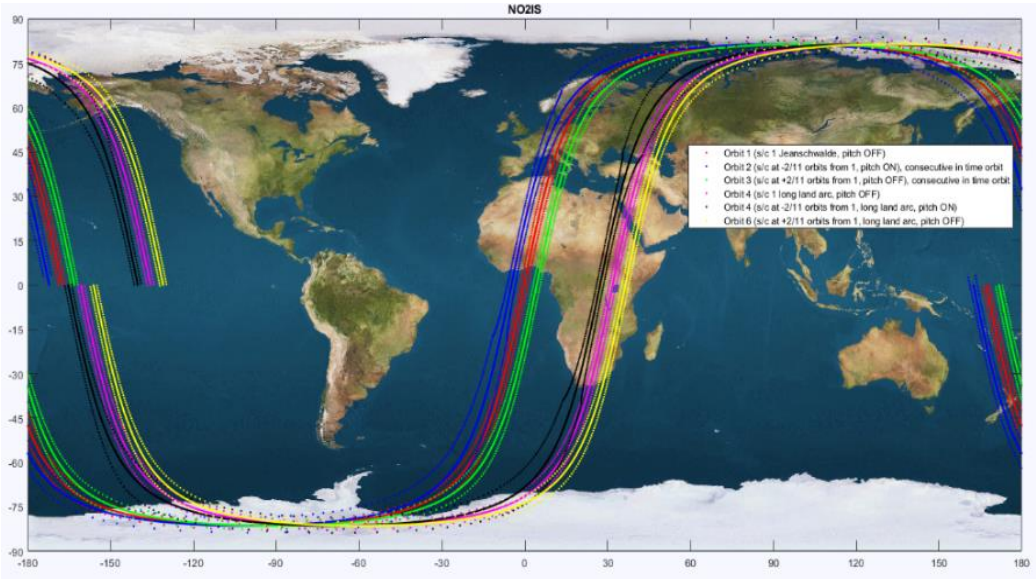

Figure 1: Illustration of the orbits provided by EUMETSAT (figure provided by EUMETSAT)

Three orbits dated on 3rd July 2025 and three dated on 23rd September 2025 are simulated. The corresponding input ancillary data to define the scene scenario are dated from 3rd July 2015 and 23rd September 2015, respectively.

The orbits (represented on Figure 1) are:

- 3rd July 2025
  - EU west (pitch on)
  - EU cent (pitch: off)
  - EU east (pitch: off)
- 23rd September 2025
  - SA cent (pitch: off)
  - SA west (pitch: on)
  - SA east (pitch: off)

For each orbit, EUMETSAT provides us with 15 L1B files (so call granule file) corresponding to day side of the orbit for both MAP and CLIM. Among all parameters included in those files, some are used as input for the test data production:

- Latitude
- Longitude
- View azimuth angle
- View zenith angle
- Solar azimuth angle
- Solar zenith angle
- Terrain height
- Land fraction (i.e. fractional coverage of land rather than water)

The used longitude and latitude parameters are given referenced to the Geoid and corrected for the intersection with the terrain, accounted for using a digital elevation model.

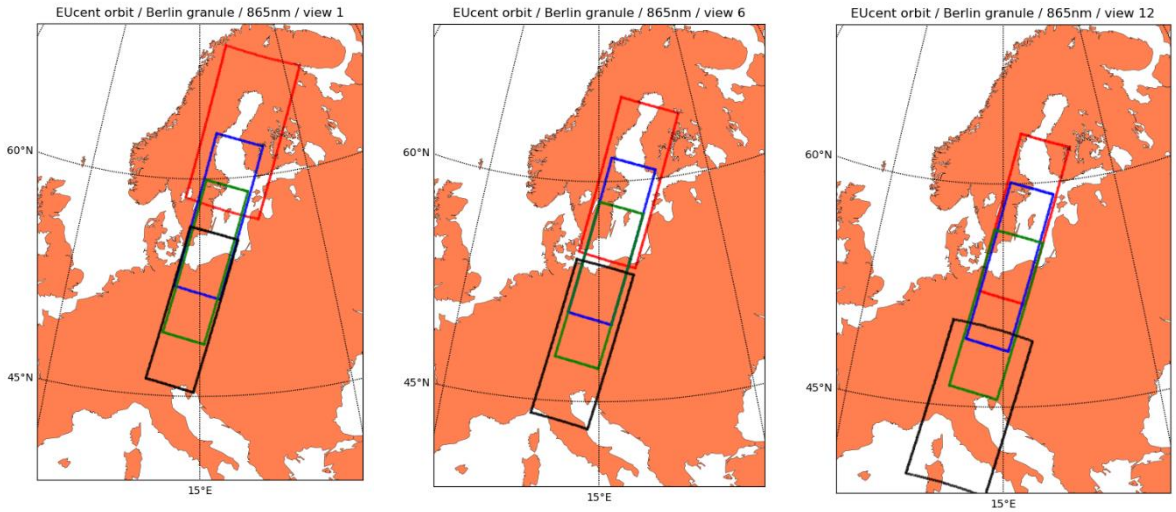

Figure 2 MAP cameras footprint from L1B file (red: camera 1, blue: camera 2, green: camera 3, black: camera 4) for granule S7A_MAP_1B_RAD_____N_20250703T111239_20250703T111539 (EUcent orbit). The three panels show three different views (view 1 for the left panel, view 6 for the middle panel and view 12 for the right panel) of channel 865 nm.

Figure 2 shows MAP cameras footprint from L1B file (red: camera 1, blue: camera 2, green: camera 3, black: camera 4) for granule S7A_MAP_1B_RAD_____N_20250703T111239_20250703T111539 (EUcent orbit). The three panels show three different views (view 1 for the left panel, view 6 for the middle panel and view 12 for the right panel) of channel 865 nm. For a granule, each camera has 12 different views that correspond to different footprints and geometries (see illustration on Figure 4). Channels of a given camera have different footprints. For a given camera / view / channel, polarizations (three Stokes parameters) are spatially collocated and have the same observing geometries.

Figure 3 shows CLIM footprint from L1B file for granule S7A_CLI_1B_RAD_____N_20250703T111237_20250703T111537 (EUcent orbit). CLIM channel 1 is red, CLIM channel 2 is blue and CLIM 3 is green. CLIM 3 is separated in three contiguous parts having its own footprint and geometry.

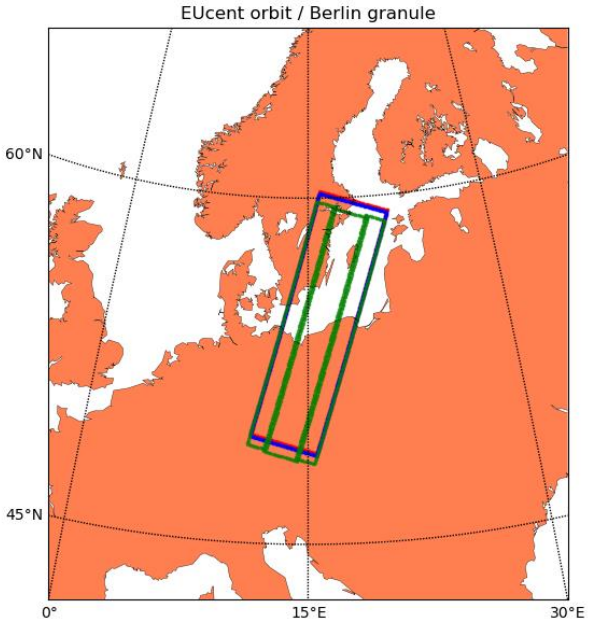

Figure 3: CLIM footprint from L1B file for granule S7A_CLI_1B_RAD_____N_20250703T111239_20250703T111539 (EUcent orbit). CLIM channel 1 is red, CLIM channel 2 is blue and CLIM 3 (a,b,c) are green.

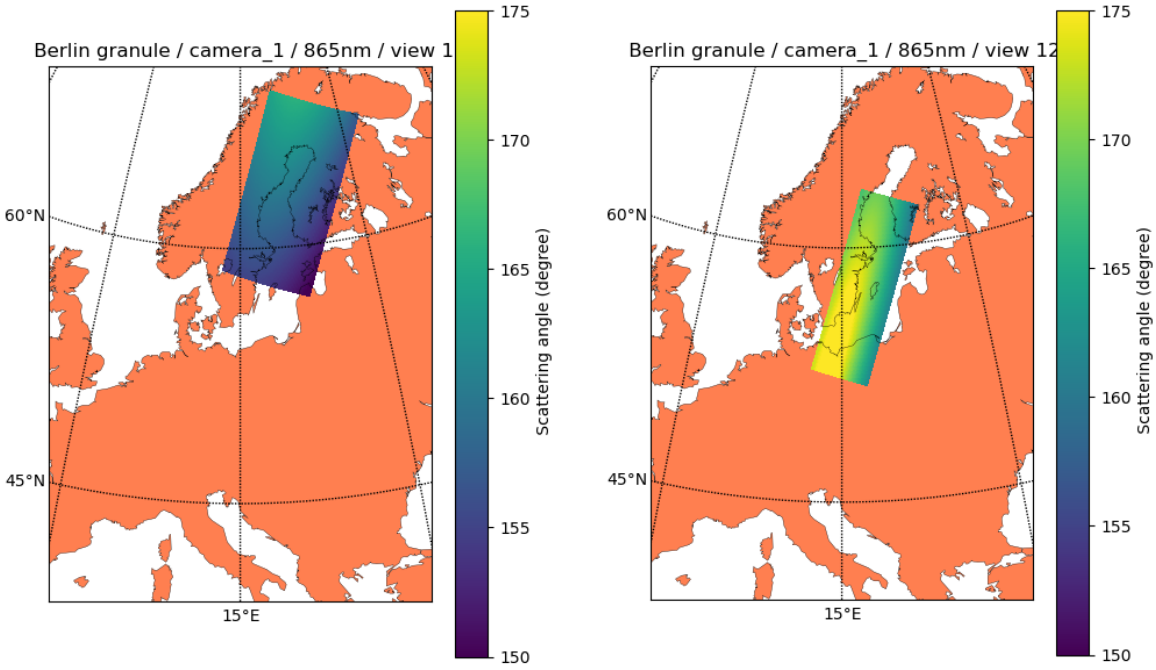

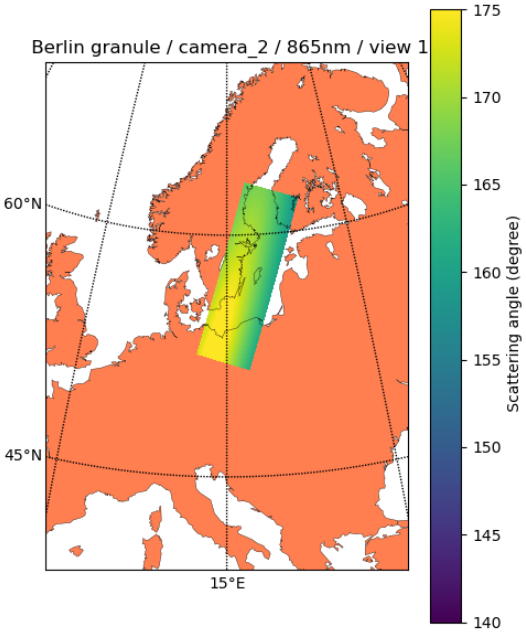
Berlin granule / camera_2 / 865nm / view 1
60°N
45°N
15°E
Scattering angle (degree)
175
170
165
160
155
150
145
140

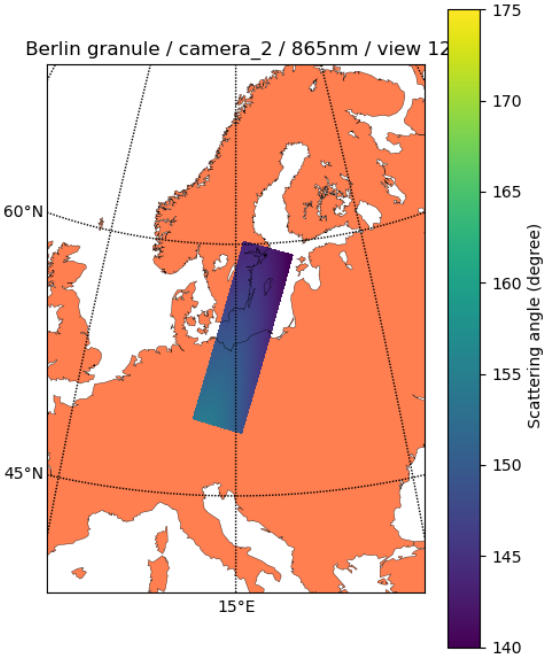
Berlin granule / camera_2 / 865nm / view 12
60°N
45°N
15°E
Scattering angle (degree)
175
170
165
160
155
150
145
140

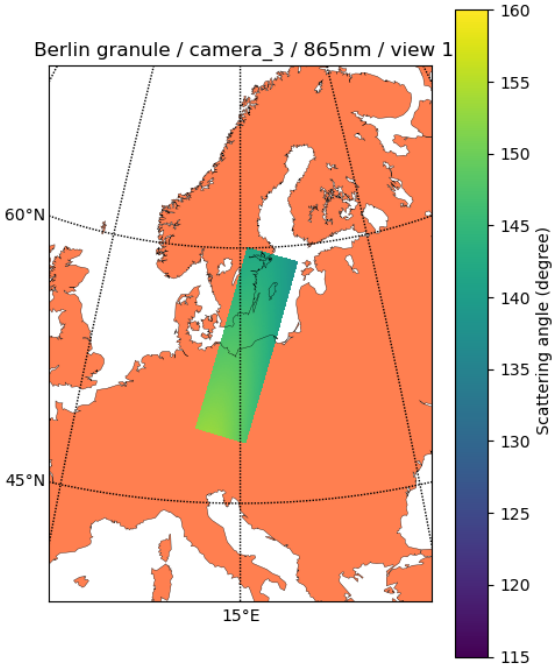
Berlin granule / camera_3 / 865nm / view 1
60°N
45°N
15°E
Scattering angle (degree)
160
155
150
145
140
135
130
125
120
115

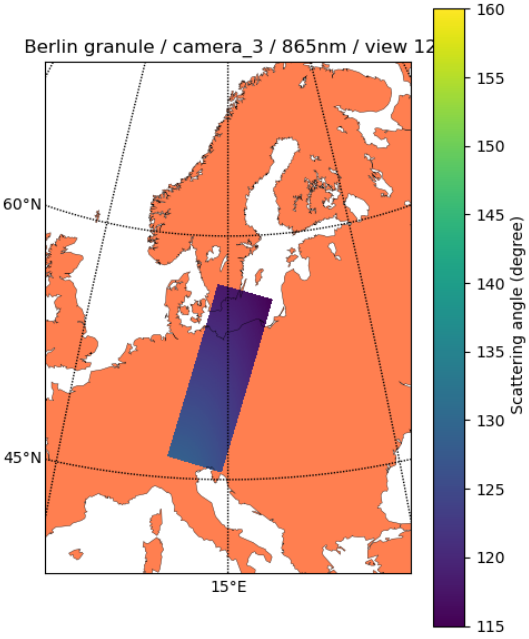
Berlin granule / camera_3 / 865nm / view 12
60°N
45°N
15°E
Scattering angle (degree)
160
155
150
145
140
135
130
125
120
115

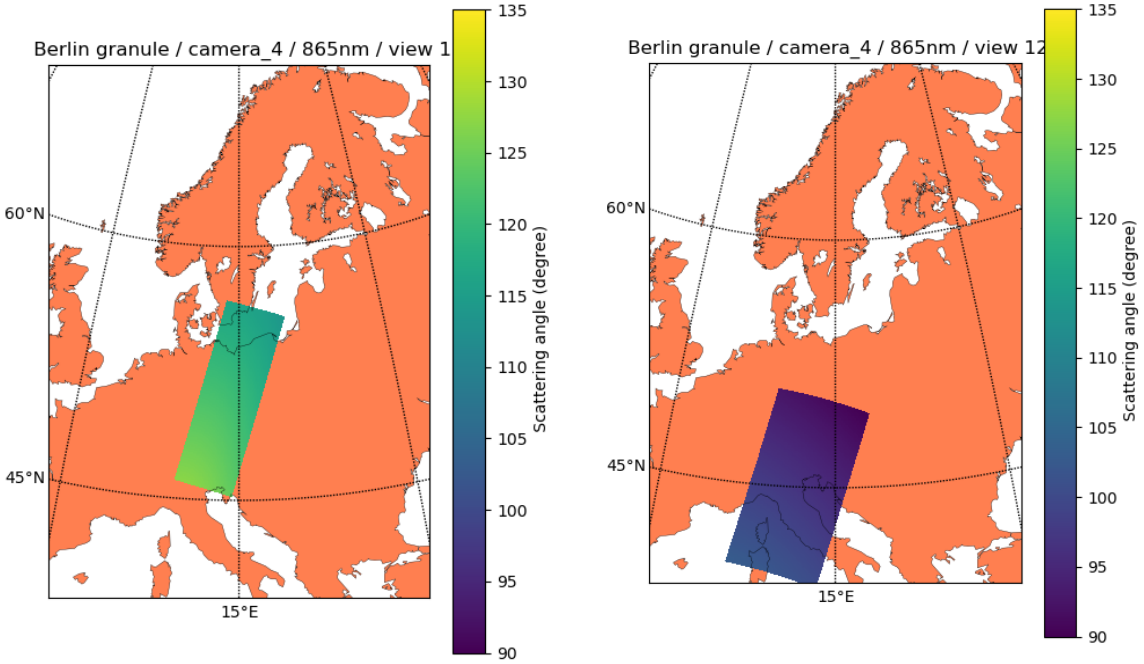

Figure 4 Scattering angles as from MAP L1B file for granule S7A_MAP_1B_RAD_____N_20250703T111239_20250703T111539 (EUcent orbit). This is plotted for the 4 cameras (along the panels row) and for view 1and 12 (left column and right column) of channel 865 nm. The plotted range of scattering angle is different for each camera but common to the two views of a given camera.

5. Input from RAL

To be as consistent as possible to the CO2I and NO2I test data, most ancillary data used to set the scene scenario are provided by RAL. Consequently, the following ancillary data description is mostly a copy (slightly adapted to our case) from RAL report on CO2I and NO2I test data (RAL, 2021). Data provided by RAL were in there native grid. This is used for both L1B MAP and CLIM and L1C MAP.

5.1. CHE model

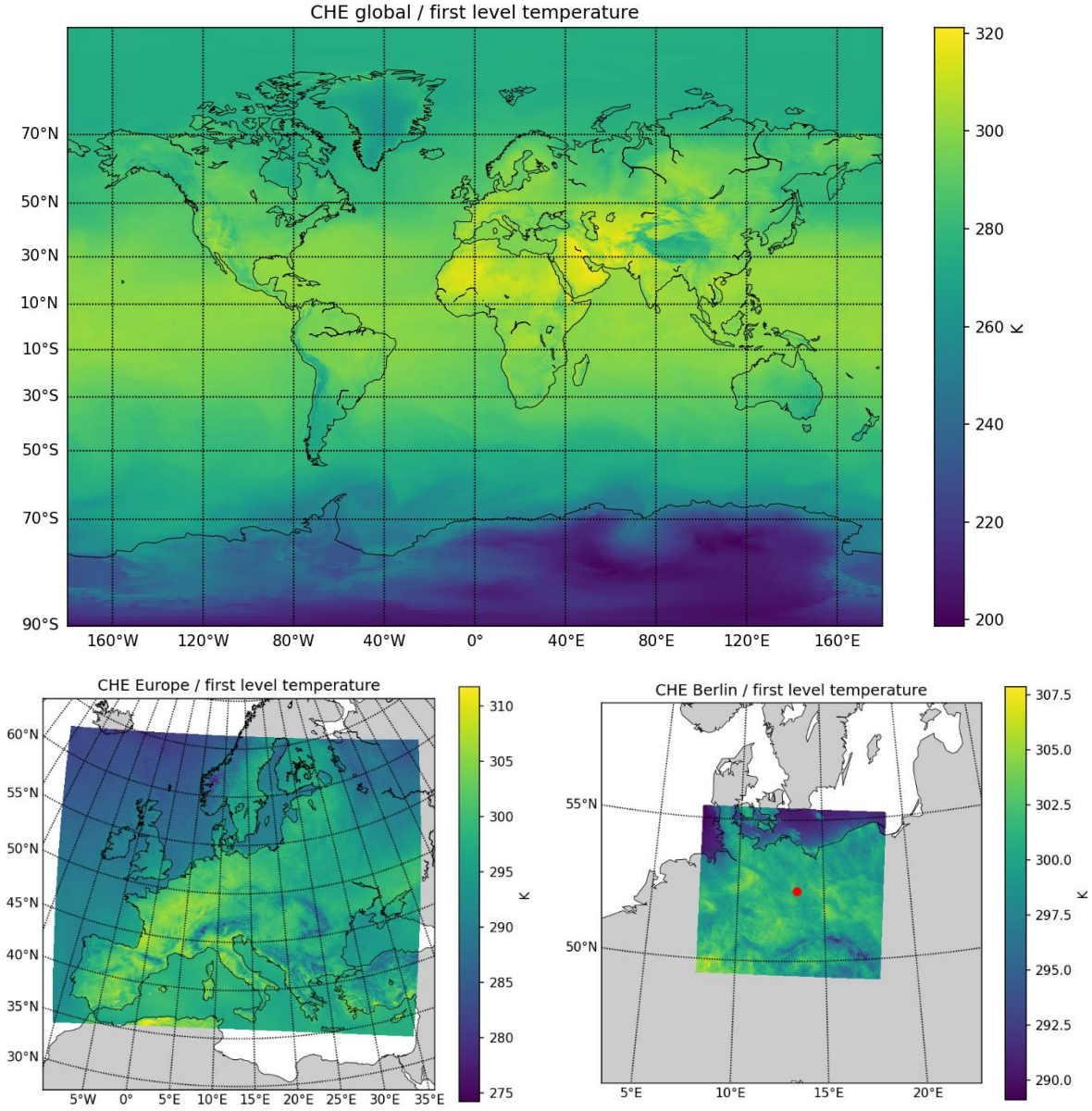

Figure 5 CHE global (upper panel), CHE Europe (lower left panel) and CHE Berlin (lower right panel) first level (closest to ground) temperature. Red point on lower left panel shows where Berlin is.

The Copernicus Atmosphere Monitoring Service (CAMS) CO2 forecasting system produce in the CO2 Human emissions (CHE) project is used. Fields for the dates required for this project were produced from several models. For v2 test data, we only use global output (produced at about 10 km spatial resolution by the ECMWF high resolution forecast model). Figure 5 shows the area where global, Europe and Berlin fields are defined.

For MAP and CLIM test data, we account for H_2O, O_2, O_3, NO_2. Other gases absorption is neglected.

The Copernicus Atmosphere Monitoring Service (CAMS) CO2 forecasting system (CHE) providing:

- The 137 levels hybrid sigma grid of the global model
- Sea ice coverage
- Snow depth
- Geopotential height profile
- 10m wind speed components (u and v)
- Surface pressure
- Profiles of CO_2, CH_4, temperature, water vapour
- Profiles of cloud liquid and ice water content

Note that at global scale, the ozone is taken from CAMS (see section 5.2). We use model fields at noon on the relevant day (e.g. 3rd July "2025"/2015).

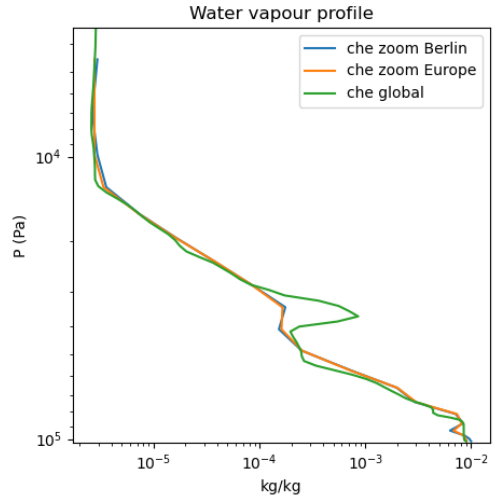

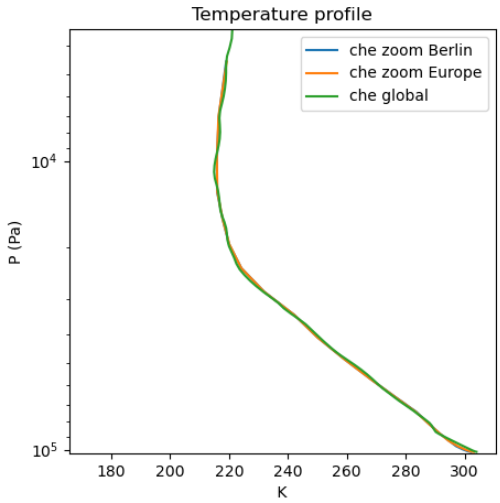

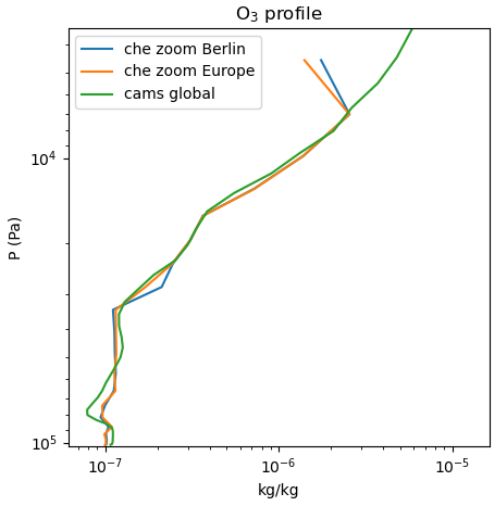

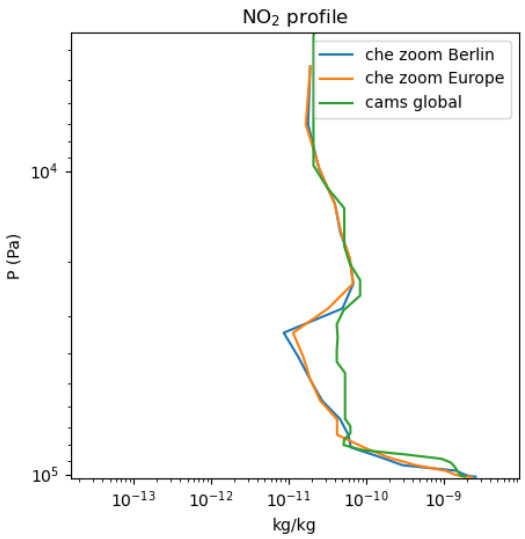

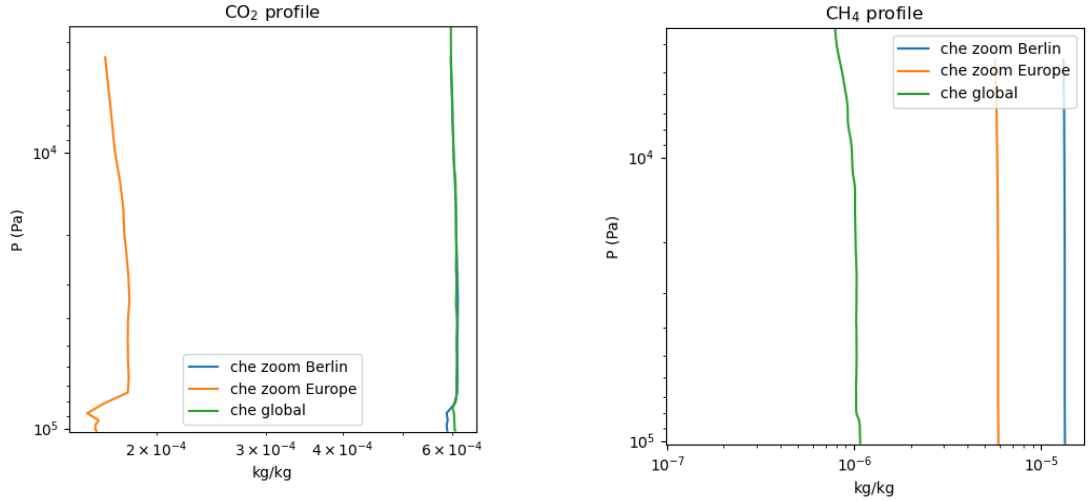

Figure 6 Water vapour (upper left), temperature (upper right), ozone (middle left), NO2 (middle left), CO2 (lower left) and CH4 (lower right) profiles as provided by CHE global, CHE Europe and CHE Berlin over Berlin (see the red dot on Figure 5). Note: for global scale, the ozone profile is provided by CAMS.

Figure 6 shows water vapour (upper left), temperature (upper right), ozone (middle left), NO_2 (middle left), CO_2 (lower left) and CH_4 (lower right) profiles as provided by CHE global, CHE Europe and CHE Berlin over Berlin (see the red dot on Figure 5). We see a rather good consistency for water vapour, temperature, ozone and NO_2 for those various datasets. Some structure in the water vapour profile is present in the global data and not in the Europe and Berlin zoom which may be related to the different vertical resolution. For the ozone profile, the cut-off at around 30 hPa in Europe and Berlin zoom may result in a lower integrated column. For the CH_4 and CO_2 profiles, we see a clear discrepancy between the global dataset and Europe and Berlin zoom.

5.2. CAMS

CAMS global reanalysis (ECMWF Atmospheric Composition Reanalysis 4) fields for the relevant day are used to supplement the CHE model fields with other needed chemical species and aerosols. It has a resolution of approximately 80 km. The following data are used:

- Aerosol component optical depth at 550nm for:
  - bcaod550 black carbon
  - duaod550 dust
  - omaod550 organic matter
  - ssaod550 sea-salt
  - suaod550 sulphate
- Total aerosol optical depth at 550 nm
- Aerosol component mass mixing ratio for:
  - aermr01 Sea salt aerosol (0.03 - 0.5 µm)
  - aermr02 Sea salt aerosol (0.5 - 5 µm)
  - aermr03 Sea salt aerosol (5 - 20 µm)
  - aermr04 Dust aerosol (0.03 - 0.55 µm)
  - aermr05 Dust aerosol (0.55 - 0.9 µm)
  - aermr06 Dust aerosol (0.9 – 20 µm)

- aermr07 Hydrophilic organic matter aerosol
- aermr08 Hydrophobic organic matter aerosol
- aermr09 Hydrophilic black carbon aerosol
- aermr10 Hydrophobic black carbon aerosol
- aermr11 Sulphate aerosol

- Profiles of ozone, NO_2

5.3. BRDF MODIS parameters

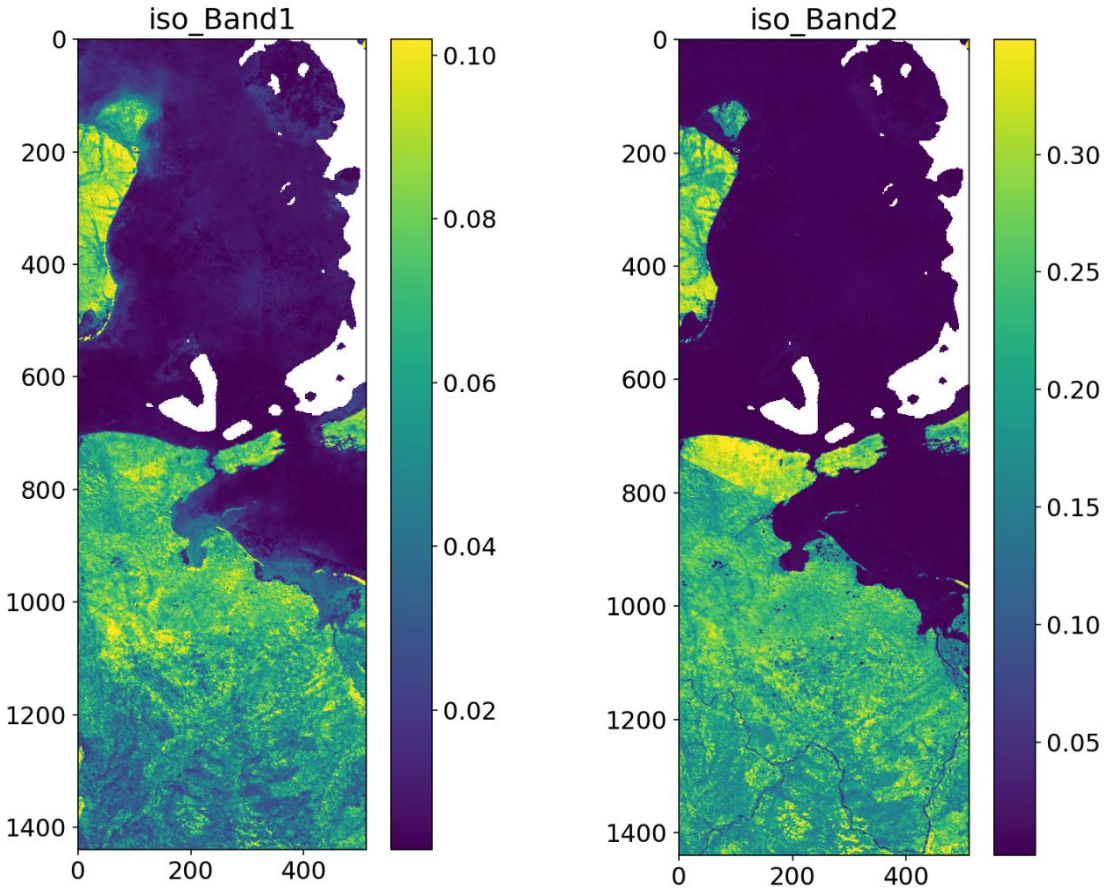

Figure 7 MCD43GF ISOMETRIC parameter for MODIS band 1 (645nm) on the left panel and MODIS band 2 (858nm) on the right panel. This is in L1B MAP grid (granule SAcent orbit, S7A_MAP_1B_N_20250923T090022_20250923T090322 camera4 view 01).

The land surface reflectance is modelled using the MODIS MCD43GF (gap-filled) product which defines (at ≈1km resolution) the coefficients of three "kernel" function (representing isotropic, geometric and volume scattering) each of which has a defined angular dependence. The parameters are only defined for 7 MODIS channels (centred at 469, 555, 659, 858.5, 1240, 1640 and 2130 nm).

We use the MODIS product defined for the relevant day, however sometimes this contains gaps particularly in the Southern hemisphere (due to high solar zenith / high cloud coverage). We therefore supplement 3rd July 2015 missing data with data from 20 Dec 2015 (missing values are filled with data from this day). Missing values in 23rd September 2015 data are supplemented with 3rd July 2015 for the Noth hemisphere and 20th Dec 2015 for South hemisphere. Figure 7 shows an example of resulting

MCD43GF ISOMETRIC parameter in L1B MAP grid. Between line 700 and 800, we clearly see a transition in band 2 (858nm) due to date change (23rd September 2015 to the South and 3rd July 2015 to the North). The transition is more visible in MODIS band 2 where the impact of vegetation is stronger.

In addition, we extend the MODIS coverage beyond the coast into the sea. This is done to avoid possible missing data around the coast arising in scenes defined as land by the L1 orbit file, as follows:

- The original fields (at 1km resolution) are convolved with a square kernel of 3x3 cells. The convolution takes account of missing data within each 3x3 area, returning the average of only the valid samples. Cells which are not defined in the original grid are filled with any valid results from the convolution (i.e. where at least one of the cells involved in the convolution was valid). This has the effect of extending valid data out to neighbouring cells (but retaining the original data where it is valid.
- This procedure is iterated with larger square kernels of dimension 5, 9 and 17 cells. Each iteration further extends the valid coverage, without replacing data filled on a previous iteration.

5.4. CCI ocean colour

BRDF over ocean is simulated as the sum of the isotropic reflectance (with transmission through the dioptre) and a surface reflectance based on the Cox and Munk model using the near surface (10m) wind speed from CHE. The water isotropic reflectance is taken from Ocean Colour CCI data. We use v4.2, monthly, 5km CCI data, which provides reflectance at 412, 443, 490, 510, 555 and 670nm.

There are significant gaps in the CCI data, which are filled as follows:

- The convolution approach described for MODIS above is applied to fill cells around the coast and any small gaps. The same convolution dimensions are used, though applied to the coarser resolution input grid (so valid data is propagated further in terms of distance on the ground).
- Any cells which are still not filled by this procedure are filled with the 2-degree latitude binned zonal mean of the (valid) reflectance data (extrapolated at fixed value to high southern latitudes where there is no ocean at any longitude). At the end of this process, a complete global field of ocean reflectance (at each wavelength) is defined.

5.5. Cloud Optical thickness

RAL computed a cloud field (cloud optical thickness) at a resolution of 1 km starting from the CHE global 10 km resolution cloud liquid and ice water content. It is derived as follow:

1. A pseudo random image (with floating point values ranging from 0-1) is generated at the 1km resolution. This is defined exactly be oversampling the grid of the CHE global model by a factor of 10. The image is generated to follow a spatial power law distribution proportional to $1/v^2$, where v is spatial wavenumber. This distribution, which gives more variability at larger spatial scales, is typical of cloud fields. The intention of the following is to use this image to define

structure at sub-CHE spatial resolution, while maintaining the larger scale structure in the CHE field.

2. A series of monotonically increasing threshold values, t_L, are defined spanning the range of optical depths. 250 values which span the optical depth range from 0.01 to 200 equally spaced in log optical depth are used.
3. For each t_L (starting at the lowest) a binary mask, M_L, is defined (at CHE resolution) with value 0 or 1 depending on whether the CHE value is larger than the threshold or not.
4. The fraction, f, of the 100 high resolution pixels within each CHE pixel which exceed the threshold is estimated. This is done by determining the fraction of the CHE data with M_L=1 in areas of 3x3 and 5x5 CHE pixels about each CHE pixel. f is estimated by extrapolating the fractions at 3x and 5x over-sampling linearly to 1 pixel sampling.
5. Within each CHE pixel, a threshold t_H, is applied to the pseudo-random image such that the fraction of high-resolution pixels which exceed t_H matches f. This is repeated for each CHE pixel, considering the corresponding 3x3 high-resolution pixels from the pseudo-random image, choosing a different threshold each time to always match the CHE pixel specific value of f. Thus, a binary mask, M_H, is generated from the high-resolution image which has the same structure as M_L at CHE resolution but has realistic structure at finer scales from the pseudo-random image. The high-scale structure tends to be continuous across CHE resolution pixels (as the pseudo-random image is continuous), though there will be discontinuities where there are strong changes in f.
6. A high-resolution image is constructed by filling an image at 1km resolution by setting all pixels where M_H=1 with the mid value between the current value of t_L and the next higher threshold value.
7. The process repeats from step 3 for each t_L in ascending order until the complete image is formed. The process results in a high-resolution image with realistic structure but digitised to only have values which are the mid-points between the chosen t_L. The levels are chosen to be sufficiently finely spaced that this does not affect the realism of the data for the intended purpose. In any case these will subsequently be interpolated spatially to the locations in the orbit files, which will largely remove any digitisation of the values.

The pseudo random cloud field generated at 1km spatial resolution has (almost) the same optical depth when degraded to the original 10 km resolution.

6. Supplementary ancillary data

6.1. IGBP classification

The land Bidirectionnal Polarization Distribution Function BPDF model is parametrized depending on the IGBP land classification. We use the MODIS MCD12Q1 yearly land classification product of 2015. This product has a nominal resolution of 500 m.

6.2. Solar spectral irradiance

Table 1 (Kurucz, 1992) solar spectrum integrated in MAP and CLIM SRF.

MAP channels	Integrated TOA downwelling solar flux (W m^{-2} μm^{-1})
0.41	1698.5
0.443	1837.4

0.49	1980.8
0.555	1869.8
0.67	1531.9
0.753	1267.7
0.865	957.15
CLIM channels	**Integrated TOA downwelling solar flux (W m^{-2} μm^{-1})**
0.67	1537.7
0.753	1267.7
1.37	362.71

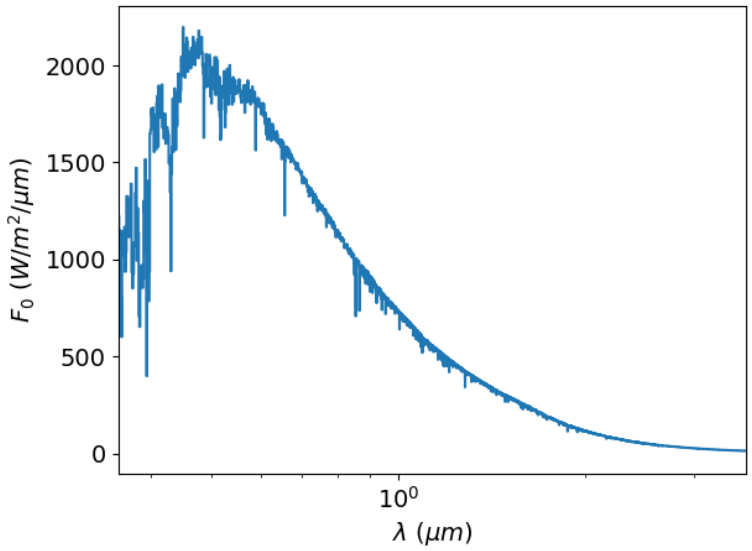

Figure 8 Solar spectral irradiance used (Kurucz, 1992)

The TOA downwelling solar flux is computed by averaging the (Kurucz, 1992) spectral flux in normalized SRF of MAP. The values of integrated flux are shown in Table 1. Note that no Sun-Earth distance factor was applied.

7. MAP and CLIM instrument assumptions

Table 2 MAP spectral characteristics from SSRD requirements

MAP spectral characteristics	
Central wavelength, λ_0 (µm)	Full Width at Half the Maximum, $FWHM_0$ (µm)
0.410	0.020
0.443	0.020
0.490	0.020
0.555	0.020
0.670	0.020
0.753	0.009
0.865	0.040

Table 3 CLIM spectral characteristics computed from the SRFs

CLIM spectral characteristics	
Central wavelength, λ_0 (µm)	Full Width at Half the Maximum, $FWHM_0$ (µm)
0.670	0.0183
0.753	0.0081
1.370	0.0144

The collocation and observation geometries for all bands and polarimeters are taken from the L1B files for both MAP and CLIM. No spatial response function is assumed: simulations are carried out using geophysical parameters interpolated to the ground-pixel centre latitude and longitude.

Despite CLIM does not measure the polarisation, we compute I, Q and U parameters for both instruments. Band spectral transmissions are assumed the same for all three Stokes parameters. The I, Q and U measurements are assumed perfectly collocated.

All pixels in L1B files for CLIM and MAP are considered up to a viewing zenith angle of 65 degrees. For larger viewing zenith angles, the data is not expected to be treated and we do not compute the corresponding signal.

The spectral, radiometric, and spatial calibration is assumed to be perfect.

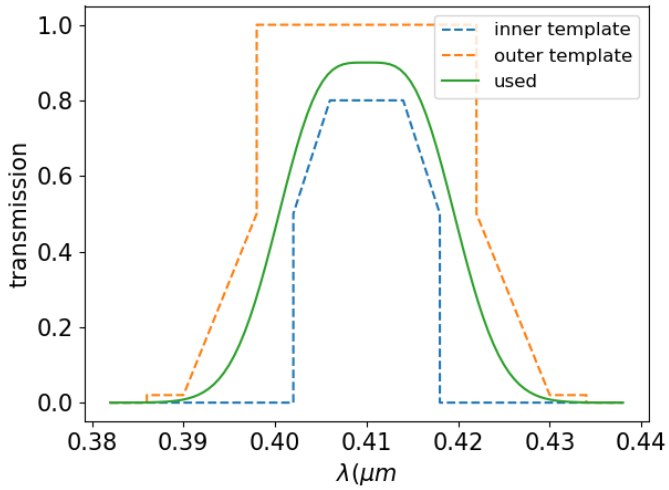

Figure 9 Spectral response function of MAP 410 nm filter. Green is the assumed SRF.

For MAP, the spectral response function is still unknown, it is assumed to be the sum of two gaussian function, so it fits in between the inner and outer template requirement. The first gaussian function has a central wavelength λ_{C1}= λ_0 + $FWHM_0/4$ and Full Width at Half the Maximum $FWHM_1$ = $FWHM_0/1.7$. The second gaussian function has λ_{C2}= λ_0 - $FWHM_0/4$ and $FWHM_2$ = $FWHM_1$ = $FWHM_0/1.7$. The resulting SRF is normalized so its peak is the mean between the outer and inner envelop peak. The spectral characteristics λ_0 and $FWHM_0$ for each MAP channel are listed on Table 2. Figure 9 shows SRF for MAP channel 1 at 0.410 microns.

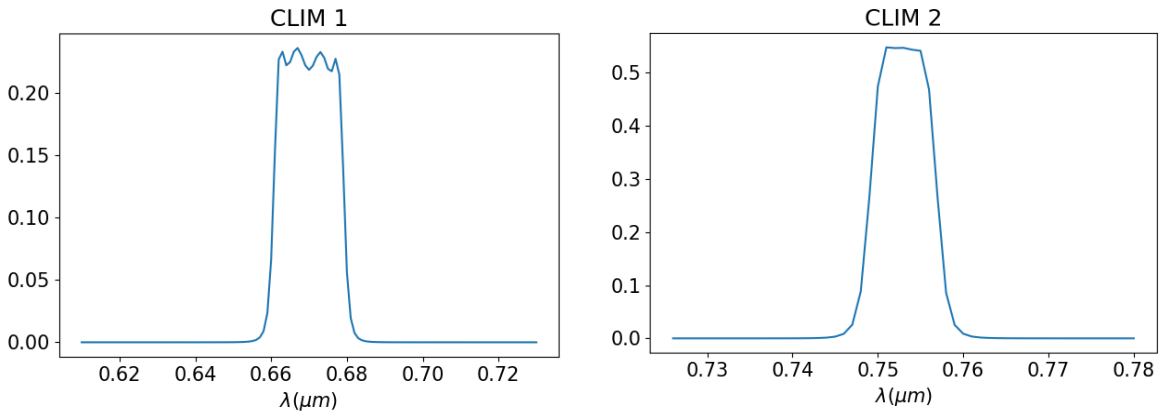

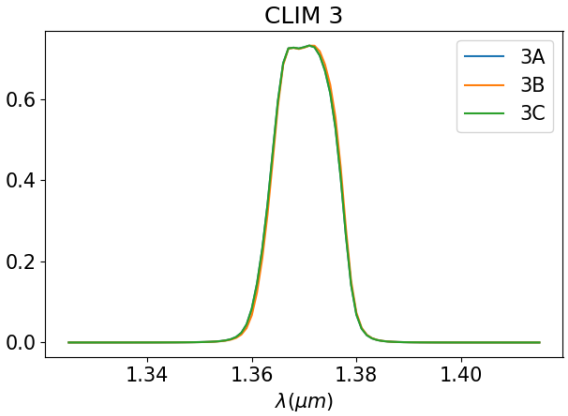

Figure 10 CLIM spectral response functions

Figure 10 shows the CLIM spectral response functions. For channel 3, while the SRFs are slightly different for A, B and C captors, we use CLIM 3B SRFs for all. Corresponding spectral characteristics are shown on Table 3.

8. Satellite radiance data simulator (SRDS)

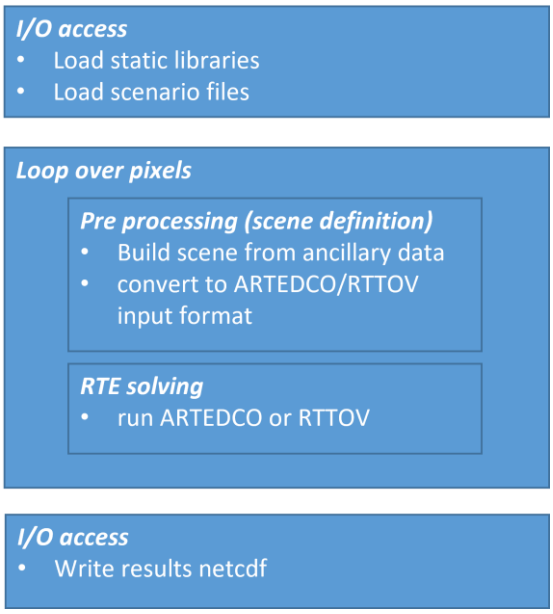

Figure 11 Schematic view of SRDS

The radiance simulator was developed by HYGEOS/LOA/ICARE through several EUMETSAT studies:

- EPS-SG 3MI & METimage test data
- Geostationary high spectral resolution test data & MTG FCI 24h test data
- MTG-IRS test data
- S7 MAP and CLIM test data

It was built to be easily applicable for any passive instruments on-board LEO and GEO satellites. It is a python 3.0 shell managing the I/O and the loop over pixel. The radiance simulator does not include any orbit propagation. It requires as an input (i) ancillary data defining the scene scenario for all pixels as well as (ii) solar/view geometries. The longitude/latitude grid used for those inputs directly fixes the grid for the output radiances. Such grid is generally given by instrument sampling through L1 files but can also be arbitrary.

The loop over pixels includes:

- the preparation of the input to the RTE solver from static libraries (e.g. cloud/aerosols optical properties, gas absorption parametrisation) and ancillary data.
- the call to the RTE through a F2PY interface (https://numpy.org/doc/stable/f2py/). The RTE solver is ran on-the-fly for every pixel. Two tools are available to solve the RTE: (i) RTTOV which is very efficient in thermal infrared to microwave spectral region or (ii) ARTDECO that is well adapted for the UV to SWIR spectral region (see section 8.1).
- Eventually the parallelization of the computation.

8.1. ARTDECO

For the present test data production, we use ARTDECO (publicly available at [Artdeco – (Atmospheric Radiative Transfer Database for Earth Climate Observation (univ-lille.fr)]) to solve RTE. ARTDECO is a

numerical tool that gathers models and data for the 1D simulation of Earth atmosphere radiances and radiative fluxes as observed with passive sensors in the UV to thermal IR range. It is developed and maintained by LOA/HYGEOS and was initially developed at LOA and funded by the TOSCA program of the French space agency (CNES). It allows one to properly account for the absorption / multiple scattering coupling in the atmosphere as well as for the surface / atmosphere coupling. The vertical distribution of aerosols and clouds can be arbitrarily defined as an input. The user can choose among available models (several methods for the truncation of the phase matrix, several RTE solver) to compute radiative quantities corresponding to the scene. Technical parameters (e.g. number of computational angles) for these models are also accessible through input files. The accuracy / computing time ratio can then be easily adjusted.

8.2. Setting for RTE solver and multiple scattering modelling

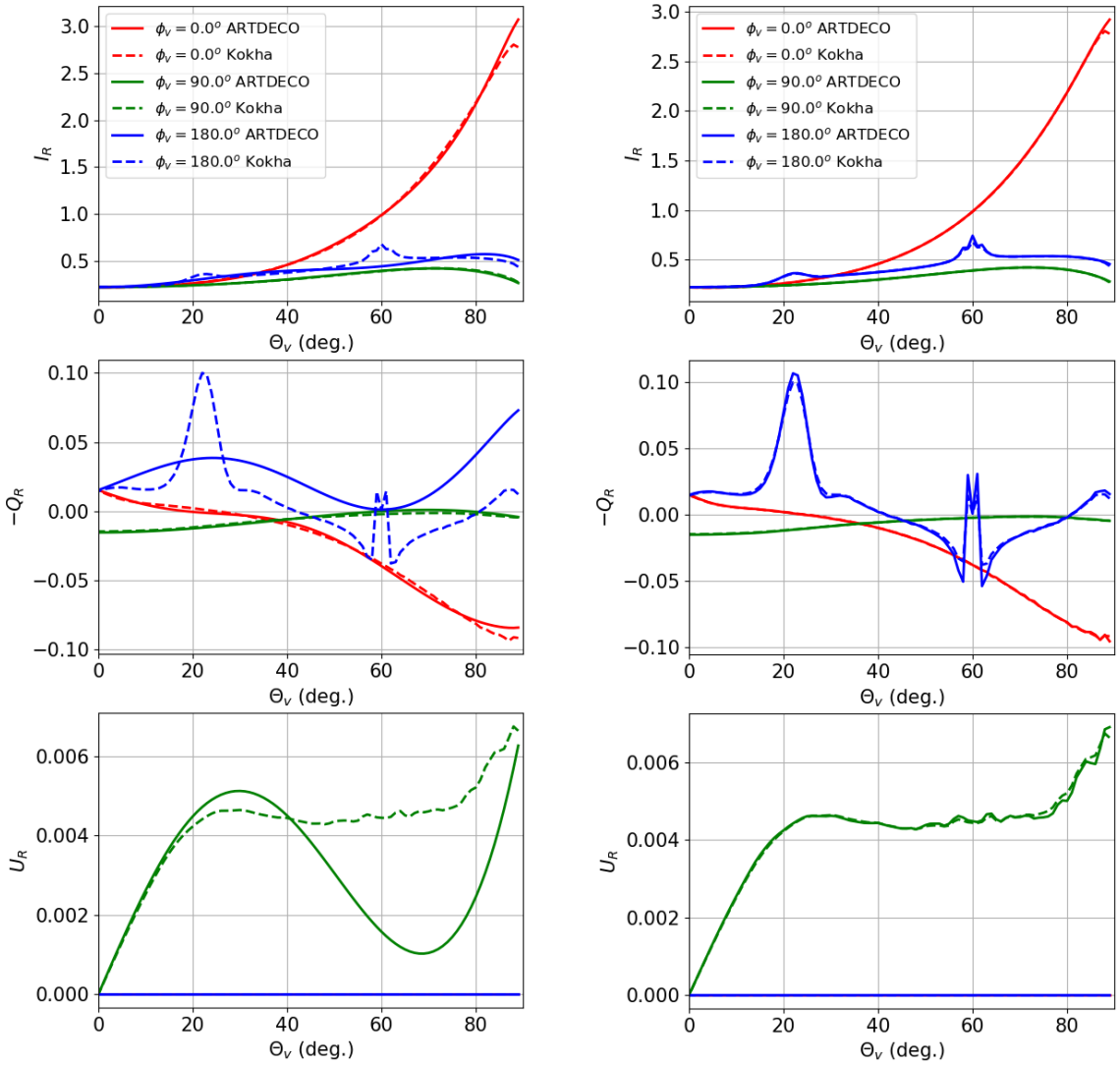

Figure 12 Illustration of the TMS benefit comparing ARTDECO to the (Kokhanovsky, et al., 2010) benchmark test for cloud scene. The dashed line is the benchmark reflectance result while the line is the ARTDECO output for 8 streams. The result is a function of the viewing zenith angle. Red, green and blue lines are for relative azimuthal angles of 0 (forward), 90 and 180 (backward) degrees. The left panel shows the results without TMS correction. The right panel show result with TMS correction.

An adding and doubling code (de Haan, Bosma, & Hovenier, 1987) is used. It accounts for the surface / atmosphere interaction through the definition of bidirectional reflectance. The first three Stokes parameters only are accounted for (I, Q, U). A semi-infinite plan-parallel geometry is assumed.

We use the Delta-M method (Wiscombe, 1977) for the truncation of aerosol and cloud phase matrix. After the RTE solving, the solar contribution to the TOA radiance is corrected for the first order scattering using the TMS method (Nakajima & Tanaka, 1988). We use the actual (tabulated) phase matrix (Buras, Dowling, & Emde, 2011) to correct radiance. This is also applied for the surface BRDF. We use 8 computational streams. Thanks to the TMS correction, we reach an accuracy on TOA radiance better than 1% for geometries out of the cloud-bow or glory (see Figure 12).

Computation of the Rayleigh optical thickness profile is implemented following (Bodhaine, Wood, Dutton, & Slusser, 1999). It formally depends on pressure, altitude, latitude, and CO_2 concentration. The dependence to latitude and CO_2 concentration are rather limited and those are fixed in the simulator to 45° and 400 ppm. The Rayleigh phase matrix is defined following (de Rooij, 1985). We use a depolarization factor of 0.0279 over the full UV-SWIR range.

We use the Ross-Li BRDF model including hot spot (Lucht, Schaaf, & Strahler, 2000). Inputs are the spectrally varying isotropic, volumetric, and geometric parameters. For the land surface polarisation, we use the BPDF model of (Maignan, Breon, Fedele, & Bouvier, 2009). It is parametrized depending on the International Geosphere–Biosphere Programme (IGBP) classification (see Figure 21).

For water surface, we use the model developed in the 6SV tool (Kotchenova & Vermote, 2007) including shadowing effect and foam contribution. We replaced the 6SV glitter model by the one described in (Mishchenko & Travis, 1997). The refractive index of water is set using a salinity of 34.3 ppt. The model accounts for under surface water reflectance (i.e. ocean colour, being an input parameter).

8.3. Setting for gas absorption parametrisation

Table 4 : Number of k-intervals used for individual gases as a function of its transmission (for airmass=2) for a standard atmosphere in PyKdis.

Transmission	Number of k-interval
0.000 - 0.050	3
0.050 - 0.500	5
0.500 - 0.800	5
0.800 – 0.900	5
0.900 – 0.990	5
0.990 – 0.999	2
0.999 – 1.000	1

The gas absorption is accounted for by applying the correlated-k technique (Lacis & Oinas, 1991), (Edwards & Francis, 2000). A specific set of coefficients was computed with our tool PyKdis for MAP and CLIM considering the SRFs described in section 7. In the solar range, the sun spectral flux is also accounted for as a weighting function to compute the coefficients.

PyKdis uses spectral gas absorption coefficients (i.e. line-by-line model) pre-computed as Look Up Tables. We use the "idealized atmosphere" line-by-line coefficients described in (Hogan & Matricardi, 2020). It was computed using version 12.8 of LBLRTM (Clough, et al., 2005) developed at Atmospheric & Environmental Research (AER). LBLRTM incorporates the self- and foreign broadened water vapour continuum via the Mlawer–Tobin–Clough–Kneizys–Davies (MT_CKD) continuum model, version 3.2 (Mlawer, et al., 2012). Continua for CO_2 and for the collision-induced bands of O_2 and N_2 are also included in the computations. Line coupling for CO_2 is treated as first order with coefficients computed as specified by (Lamouroux, et al., 2015).It should be noted, however, that line coupling coefficients for the 30012 ← 00001 and 30013 ← 00001 bands of the main isotopologue (at 6348 and 6228 cm^{-1}, respectively) have been calculated from the tridiagonal relaxation matrix parameters of (Devi, Benner, Brown, Miller, & Toth, 2007). The spectroscopic input parameters have been taken from the AER line parameter database, version 3.6, which is largely drawn from HITRAN 2012 (Rothman, et al., 2013). Gases included in this database and used for the project are for H_2O, CO_2, O_2, O_3, N_2O, N_2, CH_4.

For CO, SO_2 and NO_2, PyKdis uses the tool Py4cats (Schreier & García, 2013) to produce the LBL coefficients. We suppress the line pedestal as taken at 25 cm^{-1} from the centre. The HITRAN 2012 (Rothman, et al., 2013) database is used for line parameters. HITRAN continuum (Kochanov, et al., 2019) is added for SO_2 (Hermans, Vandaele, & Fally, 2009) and NO_2 (Vandaele, et al., 1997).

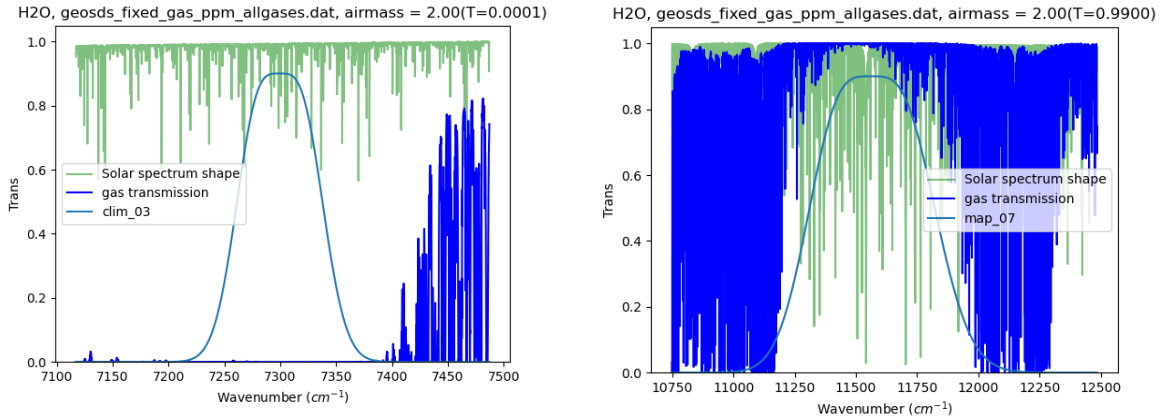

Figure 13 Example of MAP channel 7 (right panel) & CLIM channel 3 (left panel) SRFs together with normalized solar spectral flux and water vapor absorption.

Given a spectral interval (i.e. SRF range) the general principle of the k-distribution is to group all the spectral sub-intervals having similar gas transmission in groups named "bins" or "k-intervals" (k is the gas absorption coefficient), and, to associate a weight (w_i) and an absorption coefficient (k_i) to each bin i. Each bin i is therefore described by the 2-elements vector (k_i, w_i). The weight (w_i) of each bin i is proportional to the number of spectral sub-intervals associated to the bin. The advantage of it, is that

the radiative transfer code only needs to solve the RTE on each bin and not on each spectral sub-interval (as it would for line-by-line computation). We compute the TOA radiance corresponding to each k_i and combine the corresponding radiance weighted by w_i. Within a spectral interval (i.e. SRF range), the optical properties for clouds, aerosols and the Rayleigh are assumed to be constant

Because radiance computation in the solar range is CPU consuming (mostly due to multiple scattering / gas absorption coupling), to keep the number of k-interval as low as possible is necessary since it directly forces the number of calls to RTE solver. We set the number of k-interval per gas depending on the typical transmission for a standard atmosphere (see Table 4). It was tuned to keep an absolute error for transmission better or less than ≈1% for individual gas and in each spectral interval.

Table 5 Gas transmission in MAP and CLIM channels for selected gases and corresponding to an airmass of 2 for a standard atmosphere.

	MAP									
channel	**ch4**	**co**	**co2**	**n2**	**n2o**	**no2**	**o2**	**o3**	**so2**	**h2o**
0.41	1.000	1.000	1.000	1.000	1.000	0.993	1.000	1.000	1.000	1.000
0.443	1.000	1.000	1.000	1.000	1.000	0.994	0.999	0.998	1.000	1.000
0.49	1.000	1.000	1.000	1.000	1.000	0.997	0.998	0.986	1.000	1.000
0.555	1.000	1.000	1.000	1.000	1.000	0.999	0.997	0.938	1.000	0.999
0.67	1.000	1.000	1.000	1.000	1.000	1.000	0.999	0.971	1.000	0.998
0.753	1.000	1.000	1.000	1.000	1.000	1.000	0.989	0.994	1.000	1.000
0.865	1.000	1.000	1.000	1.000	1.000	1.000	1.000	0.999	1.000	0.990
	CLIM									
channel	**ch4**	**co**	**co2**	**n2**	**n2o**	**no2**	**o2**	**o3**	**so2**	**h2o**
0.67	1.000	1.000	1.000	1.000	1.000	1.000	0.999	0.971	1.000	0.998
0.753	1.000	1.000	1.000	1.000	1.000	1.000	0.989	0.994	1.000	1.000
1.37	0.995	1.000	1.000	1.000	1.000	1.000	1.000	1.000	1.000	0.000

Table 5 shows gas transmission in MAP and CLIM channels for selected gases and corresponding to an airmass of 2 for a standard atmosphere. Transmissions less than 0.999 are encountered for CH_4, H_2O, O_3, O_2 and NO_2. For CH_4 however, the transmission is 1.000 for all channels but the CLIM channel at 1.37 microns. We choose to neglect CH_4 in this channel since its impact is limited with respect to the very strong water vapour absorption. We then only consider H_2O, O_3, O_2 and NO_2 for the computation of the nominal resolution test data.

8.4. Sun induced fluorescence

The sun induced fluorescence is accounted for by adding a surface unpolarized emission in our adding and doubling code. The emitted flux is an input of ARTDECO.

8.5. Azimuth angle and polarisation convention

In ARTDECO, relative azimuth between the incoming and outgoing direction of light is considered. The relative azimuth of 0 then means forward scattering (no modification of azimuth in light propagation). Figure 14 shows the polar representation of the reflectance for I, Q, U Stokes parameters as output from ARTDECO for a sun zenith angle of 30 degrees for pure glitter situation. The Stokes vector is defined with respect to the meridian plane, which is the plane determined by the outgoing direction and the local zenith.

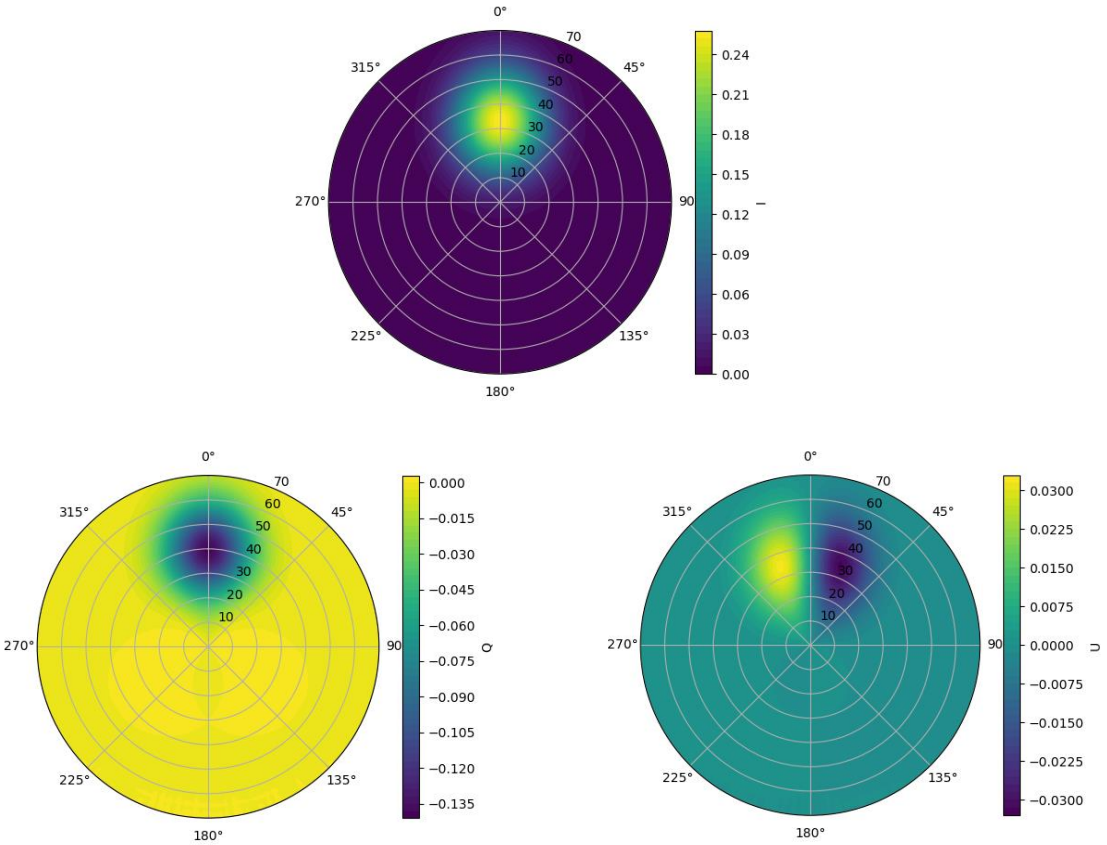

Figure 14 Polar representation of the reflectance for I, Q, U Stokes parameters as output from ARTDECO for a sun zenith angle of 30 degrees for pure glitter situation. Concentric circles represent the viewing zenith angles. The plot azimuth is the relative azimuth between the incoming and outgoing direction of light.

In MAP and CLIM L1 files, the azimuth is given from the target to the sun (sun azimuth angle, SAA) and from the target to the satellite (viewing azimuth angle, VAA). Those two angles are given East of North. To comply with the ARTDECO relative angle convention, we need to apply a rotation of 180 degree of the relative azimuth. We compute the relative azimuth angles as RAA= SAA – VAA + 180. The 180 degree rotation means a rotation of the reference plane and implies a change in U sign. This resulting convention for polarization is identical to Polder and 3MI convention.

9. Scenario setting

Ancillary data are re-gridded to the L1B pixel grid. It is used as the starting point to set each pixel's scenario that will lead to the RTE solver input.

9.1. Aerosol setting

Table 6 Relationship between aerosol optical properties (from 3MI study for relative humidity as written for each specie) and the ancillary data defining the aerosol load of the scene (CAMS data)

	Optical properties	Extinction profile		CAMS EAC4 AOD
		CAMS EAC4 mass mxing	r_{eff}(µm)	
Sea Salt	OPAC maritime clean (r_H=95%)	Sea salt (0.03 - 0.5 µm)	0.348	SSAOD550
		Sea salt (0.5 - 5 µm)	1.722	
		Sea salt (5 - 20 µm)	7.714	
Dust	Desert dust (r_H=50%)	Dust (0.03 - 0.55 µm)	0.374	DUAOD550
		Dust (0.55 - 0.9 µm)	0.704	
		Dust (0.9 – 20 µm)	2.023	
Black Carbon	OPAC continental average (r_H=50%)	Hydrophilic black carbon	0.063	BCAOD550
		Hydrophobic black carbon		
Sulphate + Organic matter	OPAC urban (r_H=50%)	Hydrophilic organic matter	0.191	OMADO550
		Hydrophobic organic matter		
		Sulphate	0.191	SUAOD550

To perform the RT calculations, optical properties need to be defined based on the mass mixing ratio profiles defined in the model fields. For aerosol these are given in terms of the CAMS aerosol components, together with their total optical depths. The RTM requires profiles of optical properties (extinction optical depth, single scatter albedo, phase matrix). The optical properties (including polarised phase function parameters) have been obtained from the 3MI/METimage study (identical to the one used for the CO2I and NO2I test data, see Figure 15). Four aerosol models are defined which are associated to CAMS aerosol types (or components) as indicated Table 6. The optical properties correspond to fixed relative humidity as shown on the same table.

Optical properties are averaged in MAP and CLIM SRFs. For the needs of spectrally oversampled test data, we duplicate the 0.41 micron wavelength point to a new point at 0.35 micron.

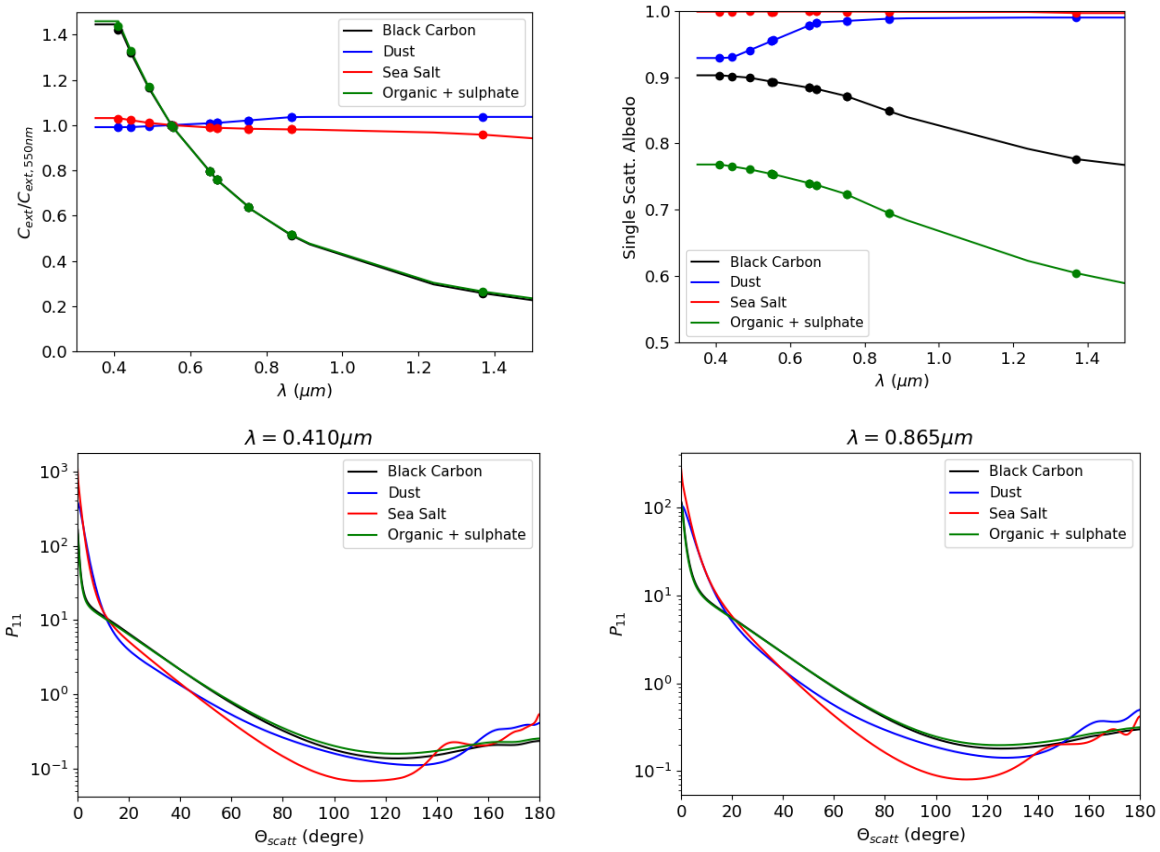

Figure 15 Aerosol optical properties. Upper left: Normalized extinction coefficient. Upper right: Single scattering albedo. Lower Left: Phase function at 0.41 microns. Lower right: Phase function at 0.865 microns.

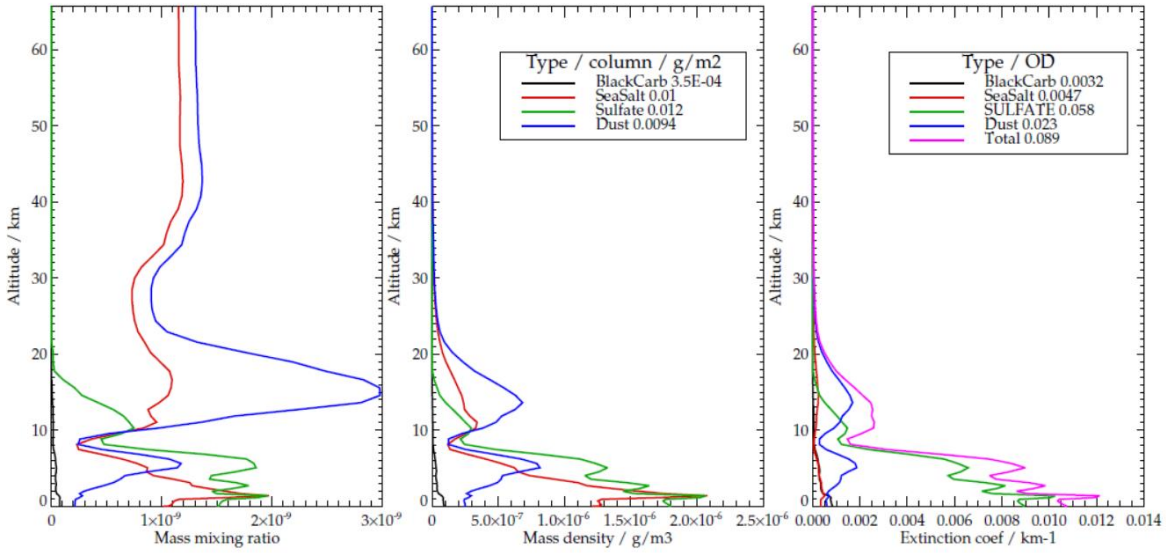

Figure 16 : Example aerosol profiles. Left hand panel shows the component mass mixing ratios from CAMS defined in the scenario file. Middle panel shows the profiles in mass density units. Right hand panel shows inferred extinction coefficient profiles. Values the legend give total column amount. The dominant aerosol class is indicated in upper case in the right-hand panel legend.

Table 7 Effective radius used for CAMS species

Aerosol	r_{eff} (µm)
Sea salt aerosol (0.03 - 0.5 µm)	0.34773817
Sea salt aerosol (0.5 - 5 µm)	1.72247235
Sea salt aerosol (5 - 20 µm)	7.71435986
Dust aerosol (0.03 - 0.55 µm)	0.37370521
Dust aerosol (0.55 - 0.9 µm)	0.7041119
Dust aerosol (0.9 – 20 µm)	2.02263818
Hydrophilic and hydrophobic organic matter aerosol	0.19077949
Hydrophilic and hydrophobic black carbon aerosol	0.06341403
Sulphate aerosol	0.19077949

The ancillary data from CAMS defines the mass mixing ratio profiles of various aerosol components, some of which are divided into size modes. The total optical depth of the components is also provided, though not for each mode. To determine the aerosol extinction coefficient profile the following approach is adopted:

- Mass mixing ratios (MMR_{aer} in kg/kg) are converted to mass density (MD_{aer} in g m^{-3}): $MD_{aer}(z) = MMR_{aer}(z)\, P(z)\, T(z)^{-1}\, r_{moist}(z)^{-1}$ with P in Pa, T in K and $r_{moist}(z) = r_{dry}\left(1 + \frac{1-\varepsilon}{\epsilon} Q(z)\right)$, where $r_{dry} = R\, m_{air}^{-1}$ and $\varepsilon = \frac{m_{h2o}}{m_{air}}$. R is the universal gas constant in J mol^{-1} K^{-1}, m_{air} and m_{h2o} are the molar mass of air and water in g mol^{-1}. *Q* is the humidity profile (kg /kg)
- An effective radius is associated to each component, with appropriate values for each mode defined based on (Reddy, et al., 2005). See Table 7.
- Mass densities are normalised by the associated effective radius. This ratio is assumed proportional to extinction profile (σ_{ext}):
  - $\sigma_{ext,BC}(z) = \alpha_{BC}\ \frac{MD_{BC}(z)}{r_{eff,BC}}$ with $MD_{BC}(z)$ being the sum of hydrophobic and hydrophilic black carbon mass density profile
  - $\sigma_{ext,SS}(z) = \alpha_{SS}\left(\frac{MD_{SS1}(z)}{r_{eff,SS1}} + \frac{MD_{SS2}(z)}{r_{eff,SS2}} + \frac{MD_{SS3}(z)}{r_{eff,SS3}}\right)$ with SS1, SS2 and SS3 being the Sea Salt bin size 1, 2 and 3 respectively.
  - $\sigma_{ext,DU}(z) = \alpha_{DU}\left(\frac{MD_{DU1}(z)}{r_{eff,DU1}} + \frac{MD_{DU2}(z)}{r_{eff,DU2}} + \frac{MD_{DU3}(z)}{r_{eff,DU3}}\right)$ with DU1, DU2 and DU3 being the dust bin size 1, 2 and 3 respectively.
  - $\sigma_{ext,SUOM}(z) = \alpha_{SUOM}\left(\frac{MD_{OM}(z)}{r_{eff,OM}} + \frac{MD_{SU}(z)}{r_{eff,SU}}\right)$ with SU being sulphate and OM being the sum of hydrophobic and hydrophilic organic matter.
- The optical depth at 550 nm of each component (AOD550) is used to scale extinction profile (σ_{ext}) :
  - $\sigma_{ext550,BC}(z) = \sigma_{ext,BC}(z)\frac{AOD_{BC550}}{\int \sigma_{ext,BC}(z)\, dz}$
  - $\sigma_{ext550,SS}(z) = \sigma_{ext,SS}(z)\frac{AOD_{SS550}}{\int \sigma_{ext,SS}(z)\, dz}$
  - $\sigma_{ext550,DU}(z) = \sigma_{ext,DU}(z)\frac{AOD_{DU550}}{\int \sigma_{ext,DU}(z)\, dz}$
  - $\sigma_{ext550,SUOM}(z) = \sigma_{ext,SUOM}(z)\frac{AOD_{SU550} + AOD_{OM550}}{\int \sigma_{ext,SUOM}(z)\, dz}$

- The extinction profile is scaled using the extinction coefficient $C_{ext}(\lambda)$ (see Figure 15, upper left panel):
  - $\sigma_{ext,BC}(\lambda, z) = \sigma_{ext550,BC}(z) \frac{C_{ext,BC}(\lambda)}{C_{ext,BC}(550\ nm)}$
  - $\sigma_{ext,SS}(\lambda, z) = \sigma_{ext550,SS}(z) \frac{C_{ext,SS}(\lambda)}{C_{ext,SS}(550\ nm)}$
  - $\sigma_{ext,DU}(\lambda, z) = \sigma_{ext550,DU}(z) \frac{C_{ext,DU}(\lambda)}{C_{ext,DU}(550\ nm)}$
  - $\sigma_{ext,SUOM}(\lambda, z) = \sigma_{ext550,SUOM}(z) \frac{C_{ext,SUOM}(\lambda)}{C_{ext,SUOM}(550\ nm)}$

Figure 16 shows an example of aerosol profiles. All four aerosol species are used and mixed at any level of the atmosphere for all RT computations. The profiles are interpolated to the 137 level of CHE.

9.2. Cloud setting

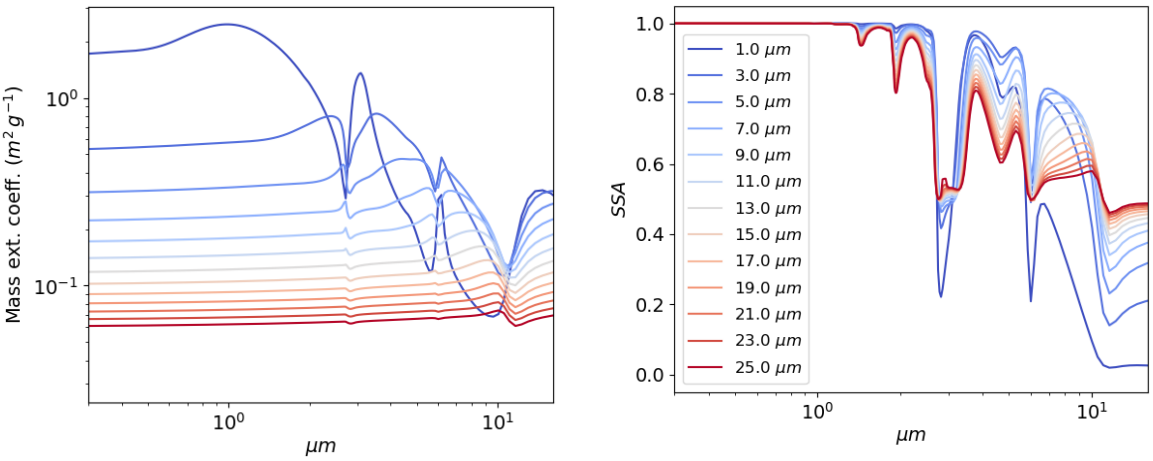

Figure 17 Mass extinction coefficient and single scattering albedo for liquid cloud for various effective radius

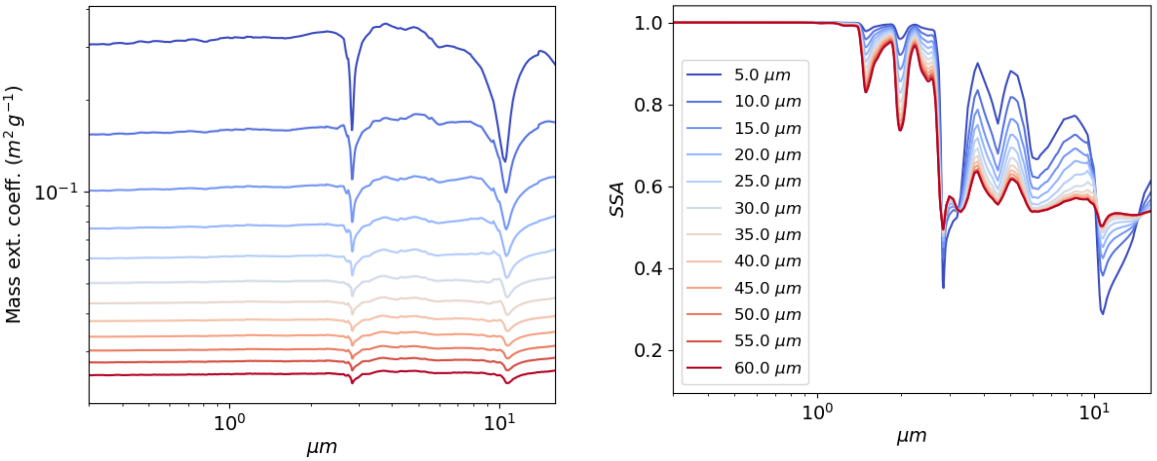

Figure 18 Mass extinction coefficient and single scattering albedo for ice cloud for various effective radius

The optical properties for ice clouds are the Global Habit Mixture of (Baum, et al., 2014). It is shown in Figure 17. The liquid cloud optical properties correspond to the library obtained from the LibRatran web site (download | libradtran). It is shown on Figure 18. Optical properties are averaged in MAP and CLIM SRFs.

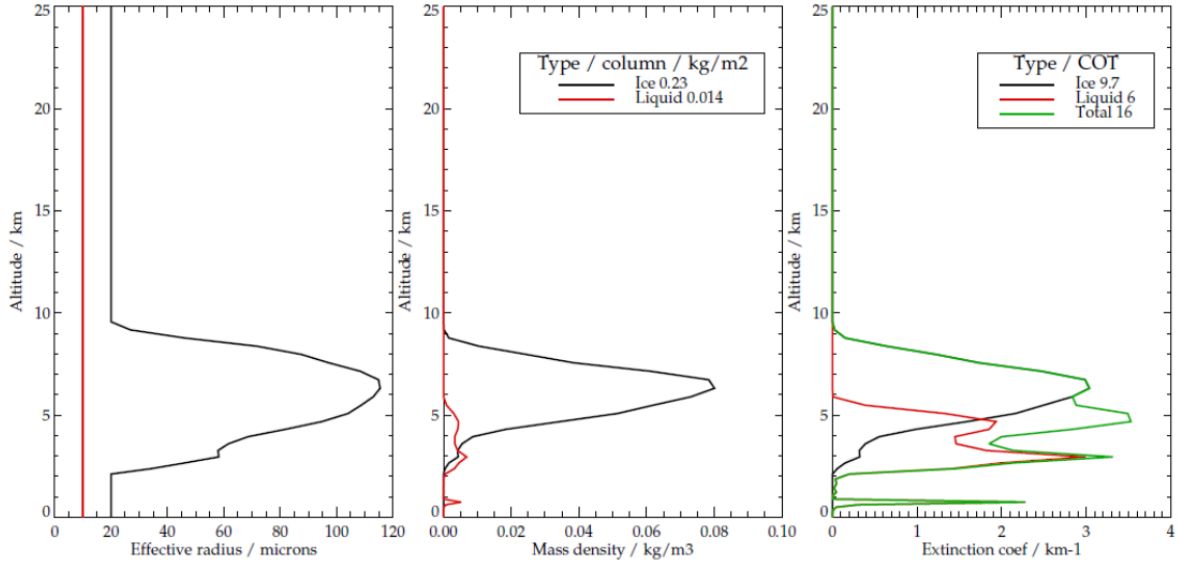

Figure 19 : Derivation of cloud extinction profiles. Left hand panel shows effective radius assigned to liquid and ice cloud. Middle panel shows the mass density profiles. Right-hand panel shows the derived extinction coefficient.

The ice cloud effective radius is assumed to vary linearly with mass density (Evans, Walter, Heymsfield, & Deeter, 1998). Liquid cloud is always assumed to have an effective radius of 10 microns.

The optical depth of liquid and ice cloud is derived from the integrated water path given by CHE global at 10 km resolution, L (in g/m^2), using the following formula (Wen & Rose, 1994), $\tau = \frac{3\,L\,Q_{EXT}}{4\,R_{eff}\rho}$ with Q_{EXT} the extinction efficiency assumed to be 2, R_{eff} the effective radius (m) and ρ the water density assumed to be 10^{-6} g/m^3. It is then normalized following the COT computed at better spatial resolution (see section 5.5). This normalization of COT profiles is performed following RAL report on CO2I and NO2I test data. Figure 19 shows an example of cloud profile.

In our simulator (for which IWC and LWC are the input), a supplementary conversion from IWC and LWC to COT is performed using the actual extinction coefficient (and not the formulation above). This leads to the total COT (ice + liquid) used for RT being different by about 3% regarding the high spatial resolution COT used for normalization.

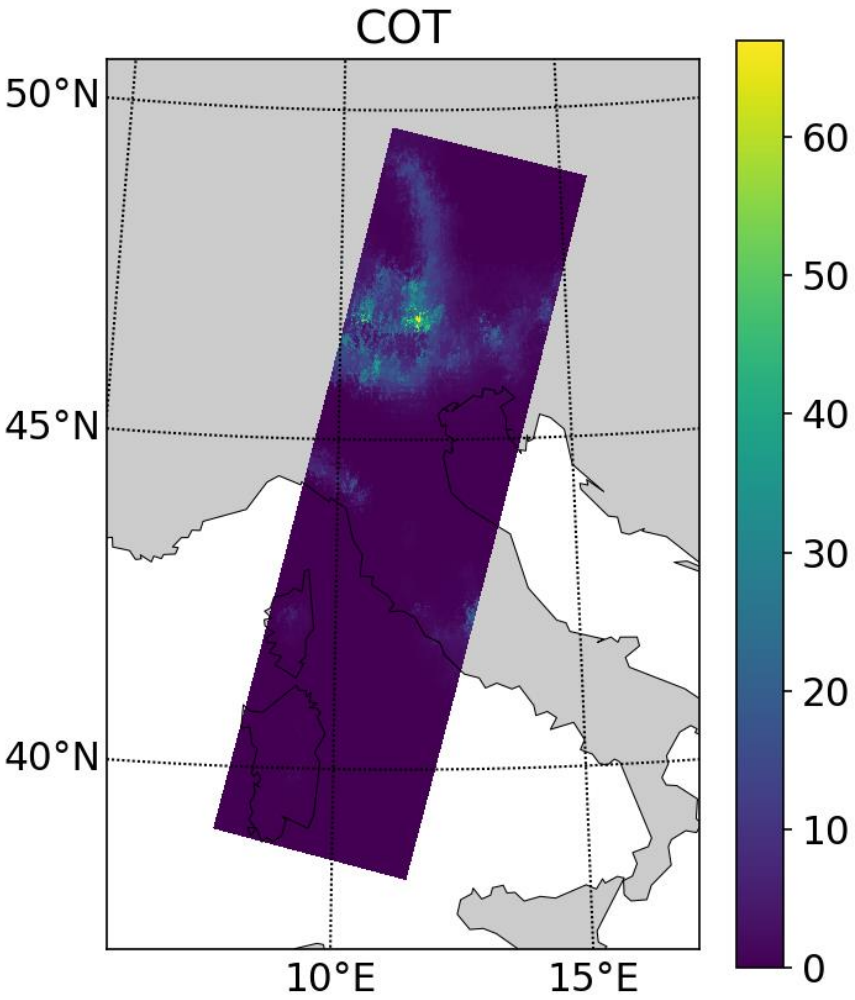

Figure 20 Example of COT ancillary (nominally at 200m) re-gridded into L1B grid of CLIM1 for granule S7A_CLI_1B_N_20250703T111537_20250703T111837.

To have spatial variability of the cloud scene down CLIM spatial scale we need to downscale the Cloud Optical Thickness provided by RAL at 1km. We apply the same method as describe on section 5.5 to set a COT field at a resolution of 200m.

The IWC and LWC as provided by CHE global at 10 km is interpolated to each pixel location and scaled according to the 200 m COT (also interpolated to the pixel location). The phase mixing and the altitude profile are left unchanged by the scaling.

9.3. Surface properties and selection rule

Table 8 Selection rules and setting for surface

	LAND	WATER	SNOW / ICE
Selection rule	if 0 > LSM ≥ 1, A land contribution is added to the pixel	if 0 ≤ LSM < 1 A water contribution is added to the pixel	if 0 < sea ice fraction ≤ 1 a sea ice fraction contribution is added to the pixel
Model	***Li Ross BRDF with Hot Spot*** • The ISO, VOL and GEO parameter (MCD43 product, nearest wavelength) ***Maignan BPDF*** • IGPB parameter (MCD12Q1) ***Sun Induced Fluorescence added***	***Sun glint (isotropic Cox and Munk) + shadowing effect + whitecaps + water reflectance*** • The wind speed (CHE global) • CCI OC data	***Li Ross BRDF with Hot Spot*** • Default ISO for snow, VOL =0 and GEO = 0 ***Maignan BPDF*** • For snow/ice ***No SIF***

The LSM is used to set surface characteristics. For MAP, a fractional LSM is provided at pixel scale. We then compute radiance for both water and land surface if LSM is not 0 nor 1. We then mix obtained radiance weighted with the LSM. For CLIM, the LSM is 0 or 1.

The IGBP classification is only used to set the BPDF.

For water/sea surface, the CHE sea ice fraction is used. If it is greater than 0, a water surface radiance and an ice/snow surface radiance are computed and corresponding radiance summed (with proper weight) at pixel scale for both MAP and CLIM.

Table 8 summarizes the selection rules and corresponding modelling for surfaces.

For snow/ice, the ISO parameters are set to

- 0.7888 at 470nm
- 0.7256 at 555nm
- 0.6749 at 659nm
- 0.6022 at 858nm
- 0.427 at 1250nm
- 0.2217 at 1640nm
- 0.1144 at 2130nm

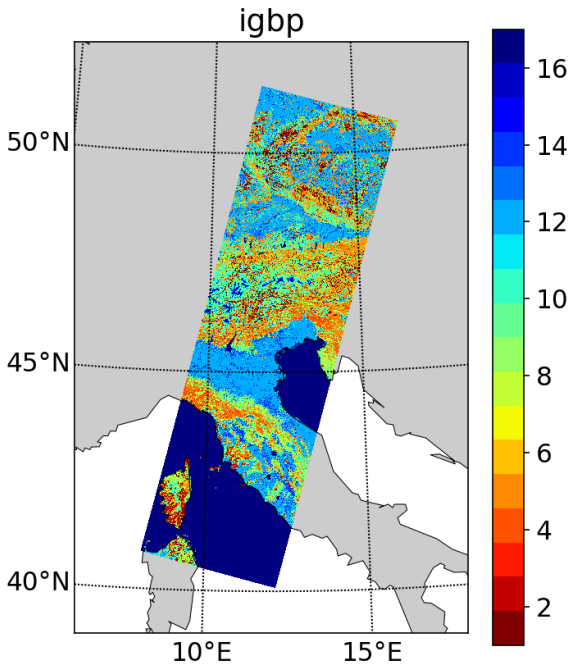

IGBP number	BPDF parameter	IGBP class
17	-	open water
19	-	coastal water
1	4.98	Evergreen needleleaf
2	7.36	Evergreen broadleaf
3	5.98	Deciduous needleleaf
4	6.87	Deciduous broadleaf
5	4.95	Mixed forest
6	4.71	Closed shrubland
7	5.99	Open shrubland
8	6.16	Wooded savanna
9	6.66	Savana Savanna
10	6.11	Grassland
11	0	Permanent wetland
12	7.58	Cropland
13	0	Urban and build
14	6.86	Crop and Nat Veg
15	7.07	Snow and ice
16	7.29	Desert

Figure 21 Left panel: Example of IGBP classification corresponding to L1B grid for camera 2 view 5 of granule S7A_MAP_1B_N_20250703T111539_20250703T111839. Right panel: IGBP number and class together with the corresponding BPDF parameter.

For the nominal spectral resolution

- Over land, the MCD43 BRDF parameters are not interpolated spectrally. The nearest neighbour is used, except for the 753 nm channel (both CLIM and MAP) that is forced to the 858 nm MODIS BRDF parameters. The BPDF parameter is set depending on the IGBP class (see Figure 21). The n_r, n_i are always set to 1.5 and 0.0, respectively. So BPDF has no spectral dependance.
- Over water, the CCI water colour is interpolated in wavelength. We add a wavelength at 900 nm with the same reflectance value than 670 nm. For wavelengths outside the range 412 to 900 nm, the reflectance is assumed to be 0

9.4. Sun induced fluorescence

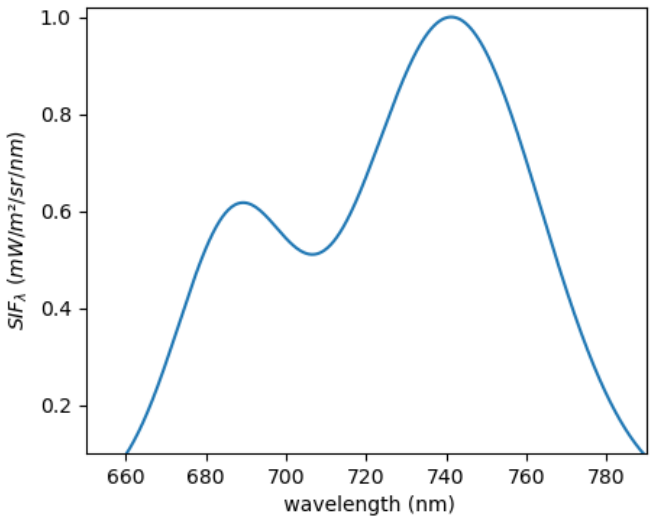

Figure 22 Fluorescence source spectrum used following (RAL, 2021). Here for SIF_λ(740nm) = 1 mW / m² / nm / sr

The Solar-Induced chlorophyll Fluorescence (SIF) is set using the linear correlation between SIF and NDVI as derived in (RAL, 2021):

SIF_λ(740 nm) = 2.15 NDVI – 0.280 mW / m² / nm / sr

with $NDVI = \frac{NIR-VIS}{NIR+VIS}$, NIR and VIS being the isotropic MCD43 MODIS BRDF parameters at 858 and 555 nm, respectively. As in (RAL, 2021), we assume that where NDVI < 0, SIF is assumed to be 0.

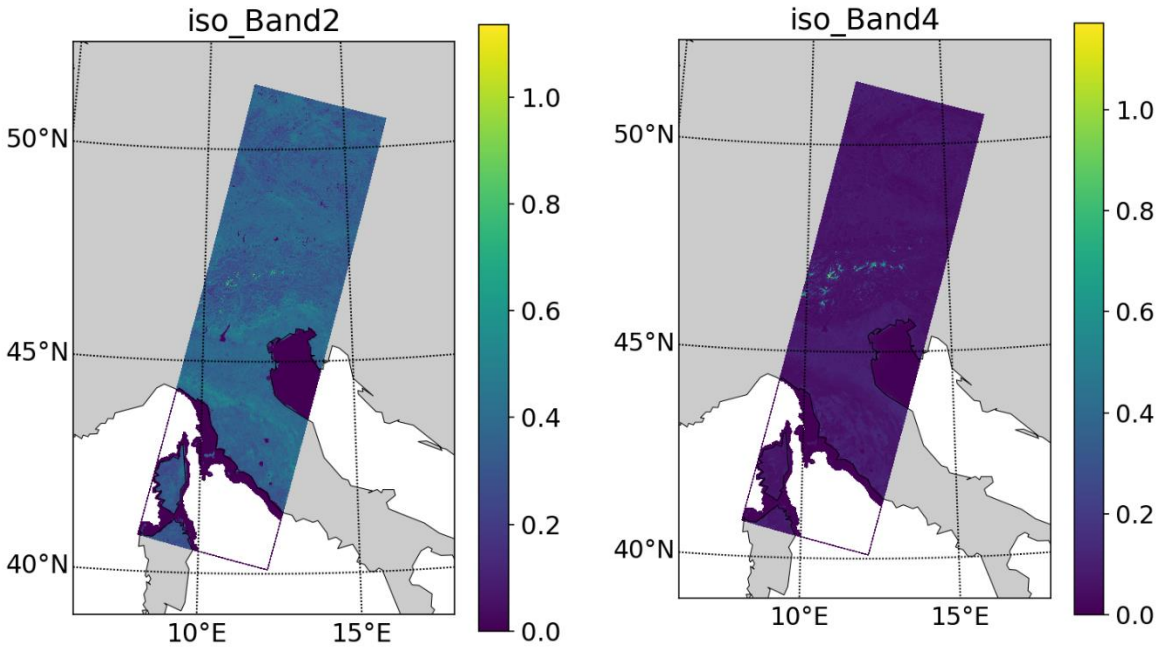

Figure 23 Example of MCD43 MODIS iso product re-gridded in L1B MAP grid for camera 2 view 5 of granule S7A_MAP_1B_N_20250703T111539_20250703T111839. Left is for MODIS channel 2 (NIR) and right is for MODIS channel 4 (VIS).

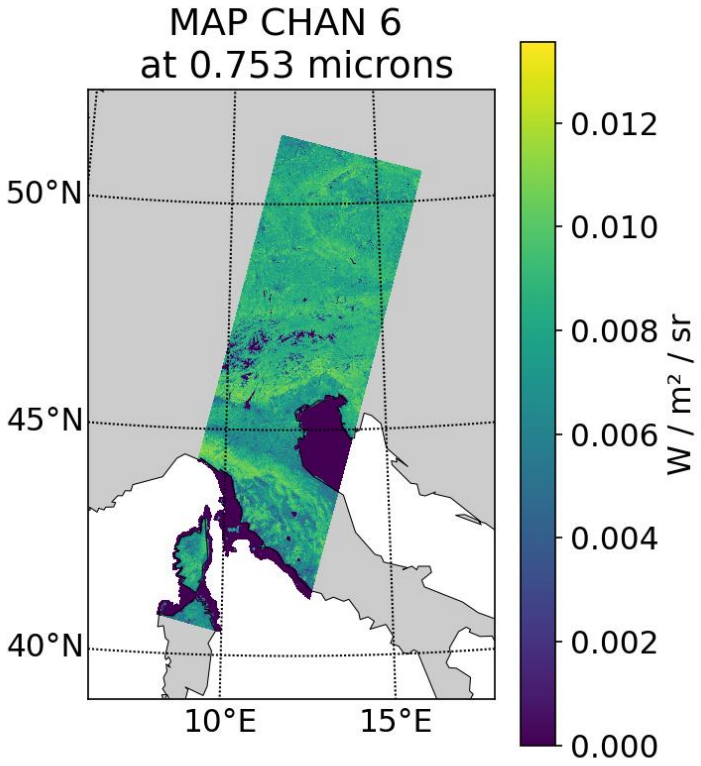

Figure 24 Example of SIF in band 6 of MAP. Grid corresponds to L1B grid for camera 2 view 5 of granule S7A_MAP_1B_N_20250703T111539_20250703T111839.

The spectral variability of the SIF is reproduced using two gaussian function as in (RAL, 2021). Figure 22 shows the fluorescence source spectrum for $SIF_\lambda(740nm)$ = 1 mW / m^2 / nm / sr. The SIF spectrum level is adjusted for any location using the $SIF_\lambda(740\ nm)$ computed from the NDVI and integrated in each MAP/CLIM SRF.

9.5. Atmosphere setting

For the nominal spectral resolution test data, we do not used the CHE zoom data. The 137 levels CHE global grid is used for computation. CAMS aerosols profiles are re-gridded on it. To save CPU while solving RTE, the number of levels is reduced by a factor of 4.

10. Production strategy

Radiance is produced for cloudy situations as defined by CHE but also for hypothetical fully clear sky situation. The Stokes parameters I, Q and U are computed in any case (including CLIM). The fourth Stokes parameter is not computed. Pixels with observation zenith angles greater than 65 degrees are ignored for computation. Such OZA occurs for MAP pitched orbits but are not likely to be used at L1C. To drop them saves CPU.

10.1. CLIM production strategy

CLIM spatial resolution is ≈90 m for CLIM 1 / 2 and ≈170 m for CLIM 3. Except for the cloud optical thickness having a spatial resolution of 200 m, ancillary data have a resolution at least about 10 times lower (e.g. MCD43 has ≈ 1km resolution). The COT being the only parameter varying at CLIM resolution scale, we can work at a lower resolution using super-pixel grid and vary COT for each super-pixel. This is equivalent to computing Look-Up Tables (LUT) of radiances as function of COT for each super-pixel and then interpolate on it to obtain the full-resolution image. If the number of sampled COT is lower than the number of full resolution pixel per super pixel, we save CPU.

The method we apply is the following:

- The super pixel grid is created by decreasing the resolution by a factor of 7 for CLIM 1 / 2 and 5 for CLIM 3. For each super-pixel, longitude, latitude, view and solar geometries, LSM and DEM are averaged.
- For each super-pixel, a sample grid of NCOT to be computed is set. Samples are linearly space in $\log_{10}$ scale going between minimum and maximum values encountered values in sub-pixels. We set $NCOT = (log_{10}COT_{max} - log_{10}COT_{min}) \times 2$ rounded to the nearest integer and with a minimum value of 2.
- All other ancillary data are re-gridded to the super-pixel grid.
- Radiance is computed for each super-pixel and each COT sample
- The full resolution radiance is obtained by interpolating in $\log_{10}$COT into super-pixel LUTs

The geometry of (observing and Solar) for a given pixel in the native grid is then slightly different than the one used for the RT computation. As a result, the sign of polarisation may be wrong (while the absolute value is close to the value that would be obtained with the exact geometry). This is especially true for U Stokes parameter for geometries close to the principal plane of scattering.

If both water and land (or snow/ice) are present within a super pixel, computation are done for each.

10.2. CPU demand

To solve the vector radiative transfer equation accounting for multiple scattering coupled with gas absorption is CPU demanding. Although some computation technics allows one to reduce it (e.g., delta-M truncation plus correction for the first order scattering, K-distribution parametrisation), the computation of MAP and CLIM test data requires the use of large numbers of CPU cores to match with a reasonable time scale for the production. The production was performed on the ICARE data centre cluster. Around 500 cores were allocated to the task. A corresponding effort in chunking the computations (getting appropriate chunk and chunk size, scripting the jobs in accordance with the cluster environment) and aggregating back the resulting radiance (to the L1B grid) was necessary.

1 680 000 cores-hours were allocated for the project to compute the 6 orbits (clear and realistic cloudy) :

- CLIM L1B : 5% of CPU demand, computed at HYGEOS
- MAP L1B : 87 % of CPU demand, computed at ICARE
- MAP L1C : 8% of CPU demand computed at HYGEOS

11. Resulting test data

11.1. MAP and CLIM L1B

The L1B files provided by EUMETSAT are filled with the computed radiance. Our simulation takes incoming fluxes listed in Table 1 as an input. It computes radiance expressed in mW m^{-2} sr^{-1} nm^{-1}. For CLIM, datasets were added for Stokes parameters Q and U in L1B files.

Figure 25 CLIM 2 (753 nm) radiance for the 3 orbits EUwest, EUcent and EUeast. Northern and southern locations on the EUwest orbit are truncated since only pixels for which OZA<65 degrees are computed. Dynamical range is between 0 and 180 mW m^{-2} sr^{-1} nm^{-1}.

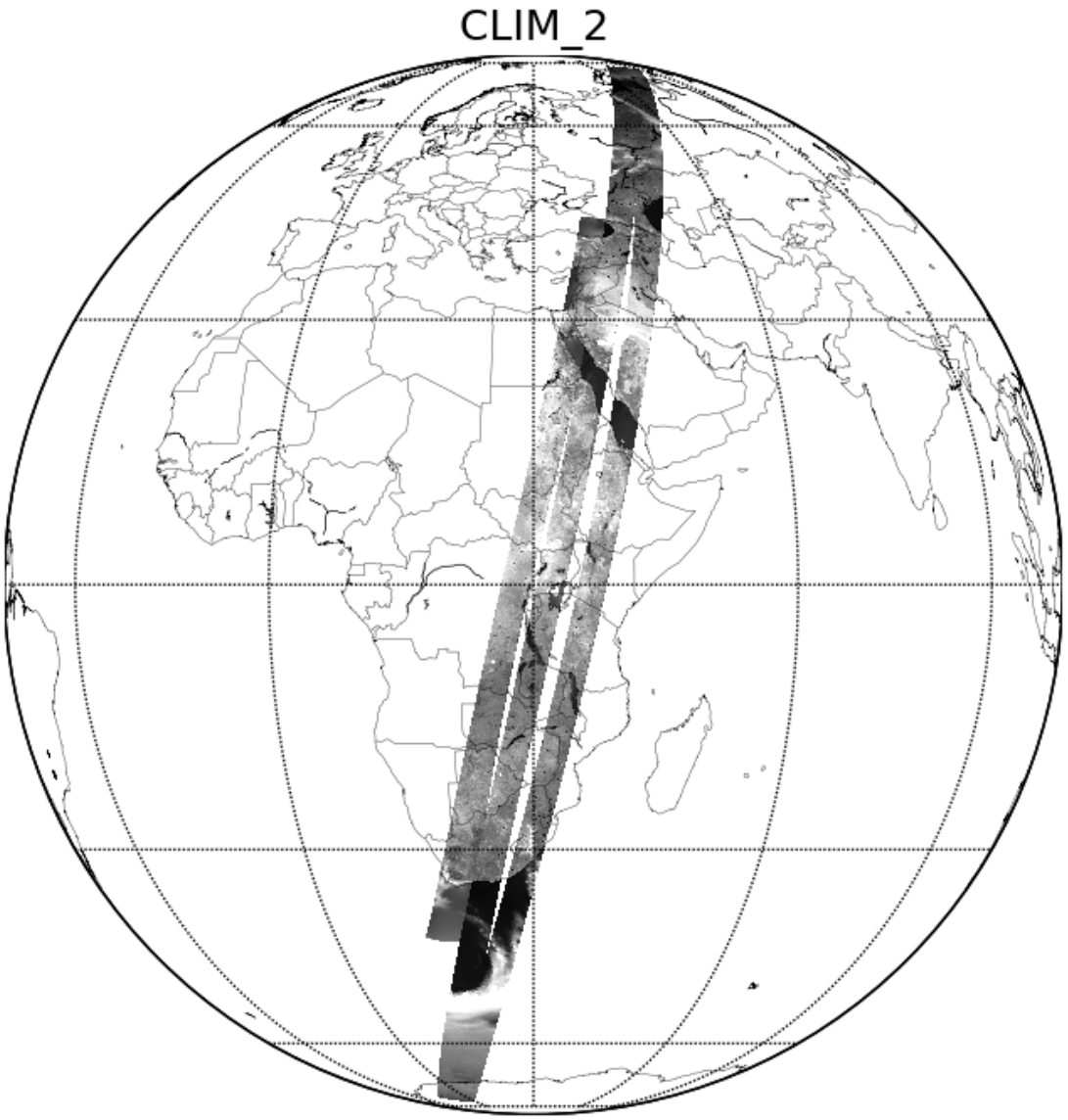

Figure 26 CLIM 2 (753 nm) radiance for the 3 orbits SAwest, SAcent and SAeast. Northern and southern locations on the SAwest orbit are truncated since only pixels for which OZA<65 degrees are computed. Dynamical range is between 0 and 180 mW m^{-2} sr^{-1} nm^{-1}.

Figure 25 and Figure 26 present a global view of the 6 computed orbits as seen with CLIM 2. We see that the test data covers a wide range of conditions in terms of cloudiness and surface conditions. The Surface is quite brighter than in V1 test data due to the new setting of the BRDF parameter being forced to the 858 nm MODIS channel, on the red side of the red edge.

Figure 27 shows radiance (I, Q, U Stokes parameters), and corresponding histogram, computed for granule S7A_MAP_1B_RAD_____N_20250703T111539_20250703T111839 (part of EUcent Nadir mode orbit) for channel 1 (410 nm) / camera 2 / view 6. Figure 28 shows the same for full clear sky assumption. The surface appears dark with respect to the clouds. The minimum radiance of 67 mW

m^{-2} sr^{-1} nm^{-1} is related to the Rayleigh scattering that is significant at that wavelength also causing the strong polarization of the signal toward the North-East corner.

Figure 29 shows radiance (I, Q, U Stokes parameters), and corresponding histogram, computed for granule S7A_MAP_1B_RAD_____N_20250703T111539_20250703T111839 (part of EUcent Nadir mode orbit) for channel 7 (865 nm) / camera 2 / view 6. Figure 30 shows the same for full clear sky assumption. The contrast between the surface and cloud is lower than for channel 1 due to the greater surface reflectance at that wavelength. The Rayleigh scattering and water (far from glint) reflectance being low, the minimum radiance is relatively lower than for channel 1. The polarization towards cloudy pixels clearly reveals the presence of ice phase that depolarizes the signal.

Figure 31 shows radiance (I, Q and U Stokes parameters), and corresponding histogram, computed for granule S7A_CLI_1B_RAD_____N_20250703T111539_20250703T111839 (part of EUcent Nadir mode orbit) for CLIM channel 1 (670 nm). Figure 32 shows the same for full clear sky assumption.

Figure 33 shows radiance (I, Q and U Stokes parameters), and corresponding histogram, computed for granule S7A_CLI_1B_RAD_____N_20250703T111539_20250703T111839 (part of EUcent Nadir mode orbit) for CLIM channel 3B (1370 nm). Channel 3A and 3C (not shown here) look very similar and are just extension of 3B on the sides in across track direction. For channel 3, we do not show full clear sky assumption since the strong water absorption block all signal from the surface.

Figure 34 shows radiance (I, Q and U Stokes parameters), and corresponding histogram, computed for granule S7A_CLI_1B_RAD_____OP_20250703T113347_20250703T113647 (part of EUwest pitched mode orbit) for CLIM channel 1 (670 nm). We see a strong contribution of the glint toward water surface pixels in that pitched mode. It is especially striking in polarisation.

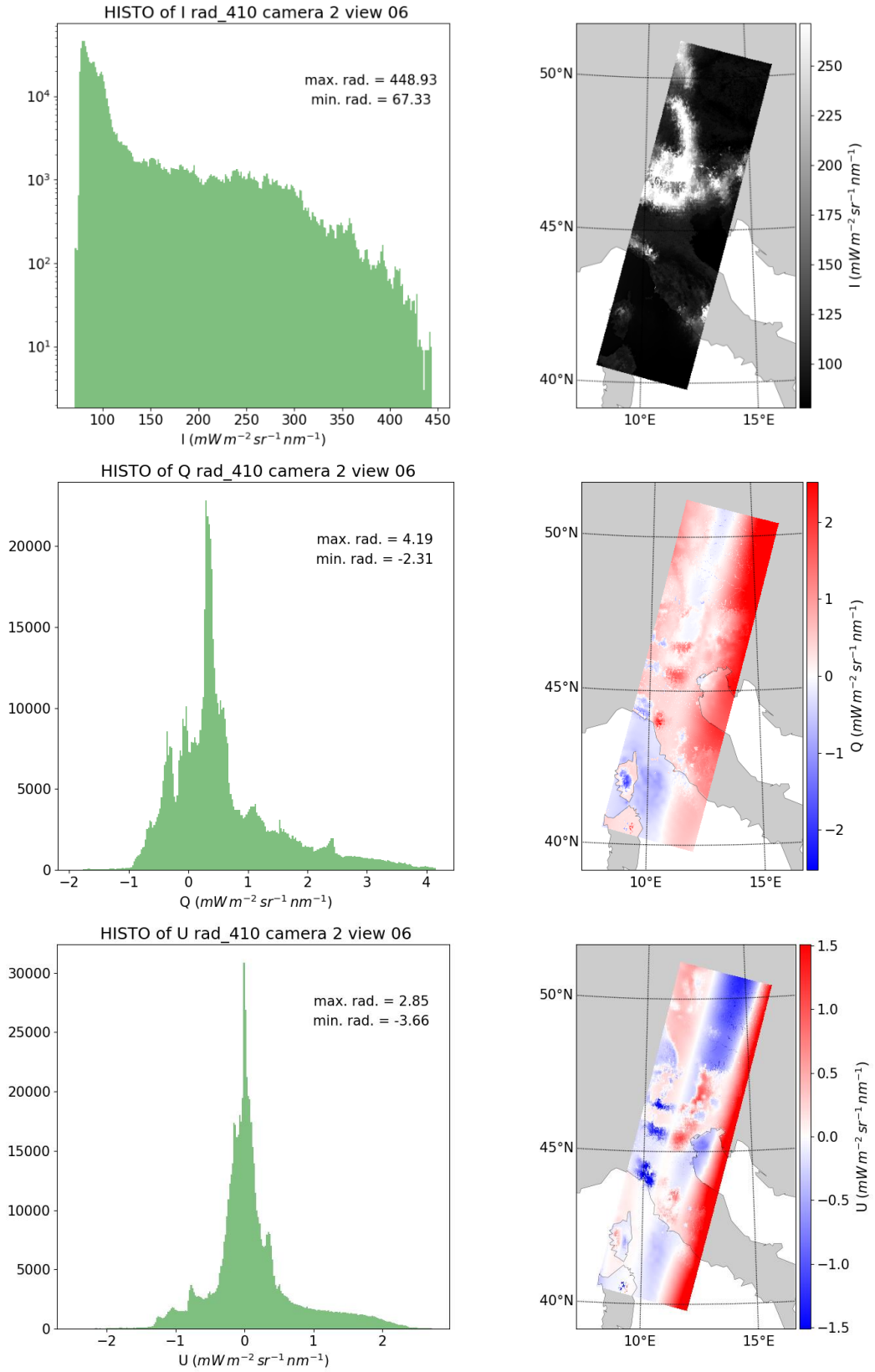

Figure 27 Radiance, and corresponding histogram, computed for granule S7A_MAP_1B_RAD_____N_20250703T111539_20250703T111839 (part of EUcent Nadir mode orbit) for channel 1 (410 nm) / camera 2 / view 6. Upper panel, middle panel and lower panel show I, Q and U Stokes parameters respectively.

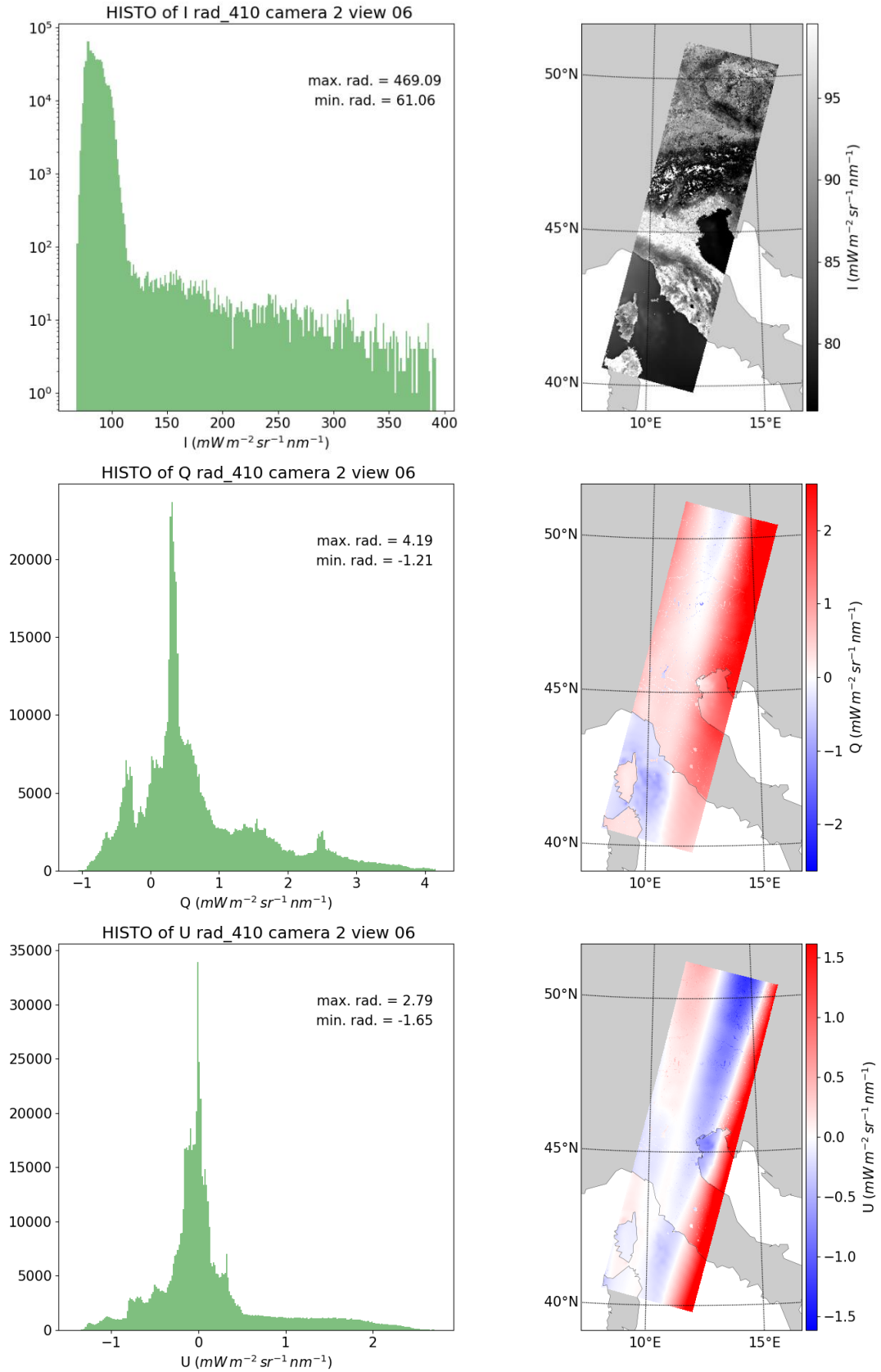

Figure 28 Radiance, and corresponding histogram, computed for granule S7A_MAP_1B_RAD_____N_20250703T111539_20250703T111839 (part of EUcent Nadir mode orbit) for channel 1 (410 nm) / camera 2 / view 6 assuming a full clear sky situation. Upper panel, middle panel and lower panel show I, Q and U Stokes parameters respectively.

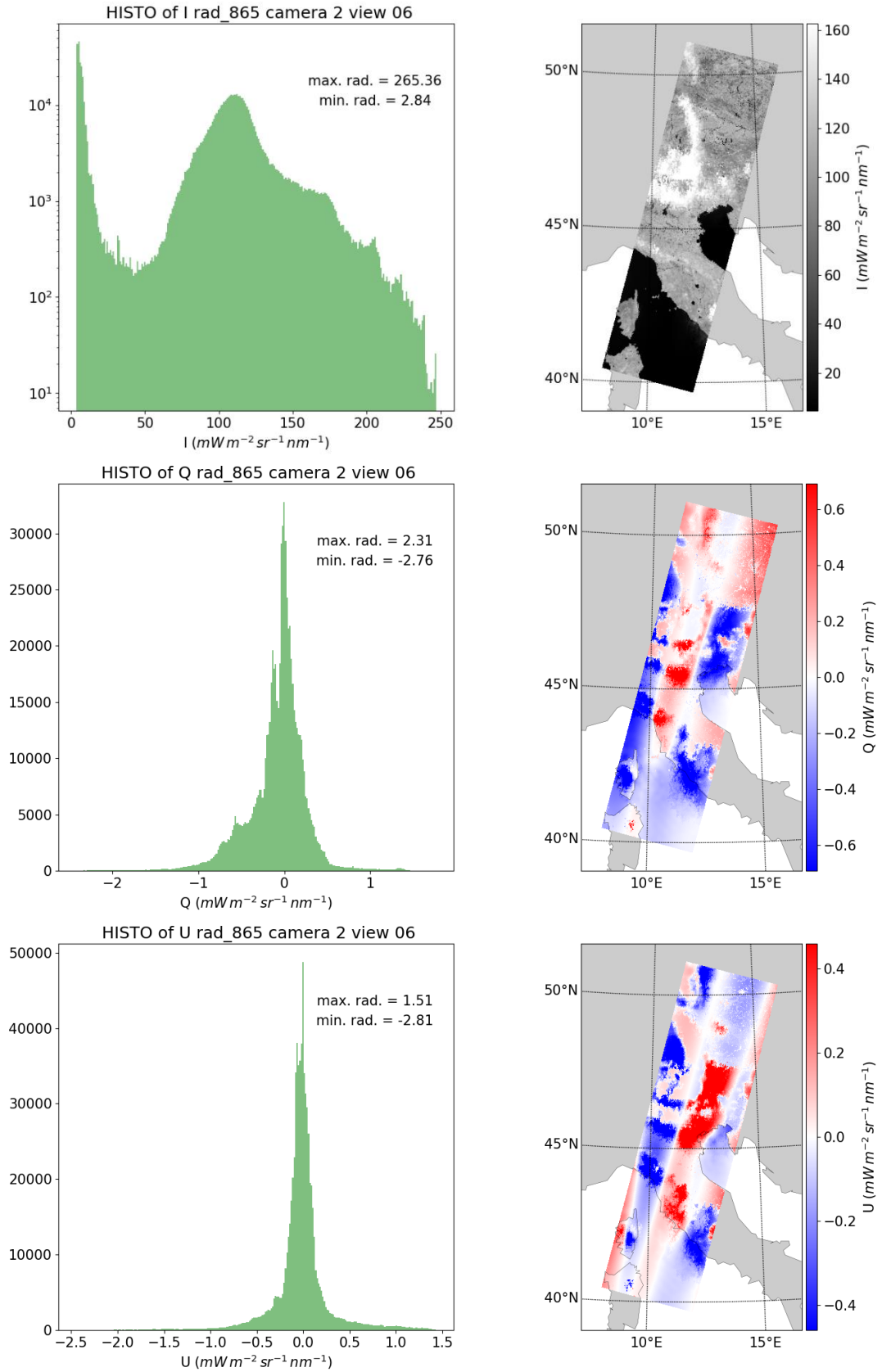

Figure 29 Radiance, and corresponding histogram, computed for granule S7A_MAP_1B_RAD_____N_20250703T111539_20250703T111839 (part of EUcent Nadir mode orbit) for channel 7 (865 nm) / camera 2 / view 6. Upper panel, middle panel and lower panel show I, Q and U Stokes parameters respectively.

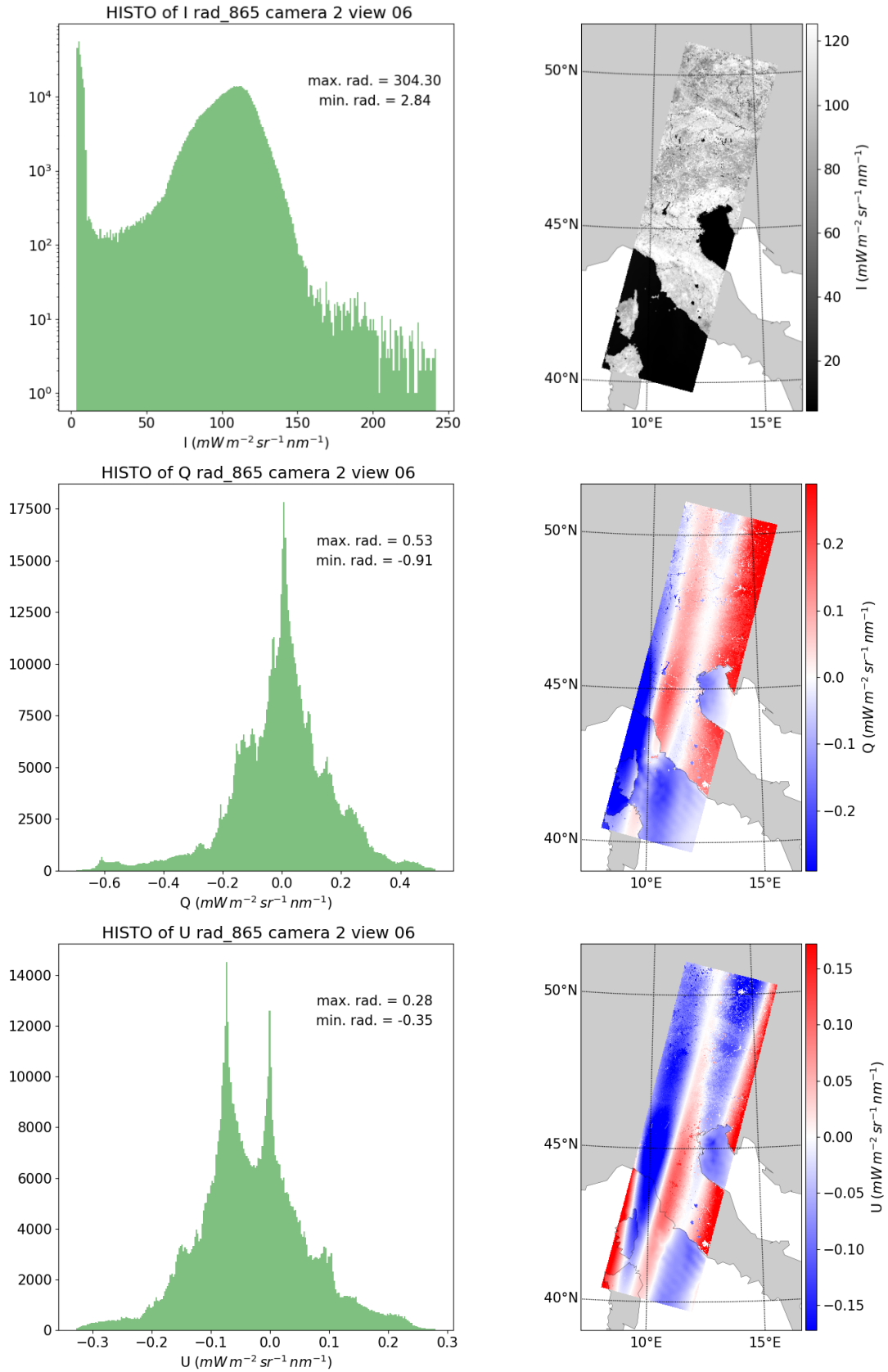

Figure 30 Radiance, and corresponding histogram, computed for granule S7A_MAP_1B_RAD_____N_20250703T111539_20250703T111839 (part of EUcent Nadir mode orbit) for channel 7 (865 nm) / camera 2 / view 6 assuming a full clear sky situation. Upper panel, middle panel and lower panel show I, Q and U Stokes parameters respectively.

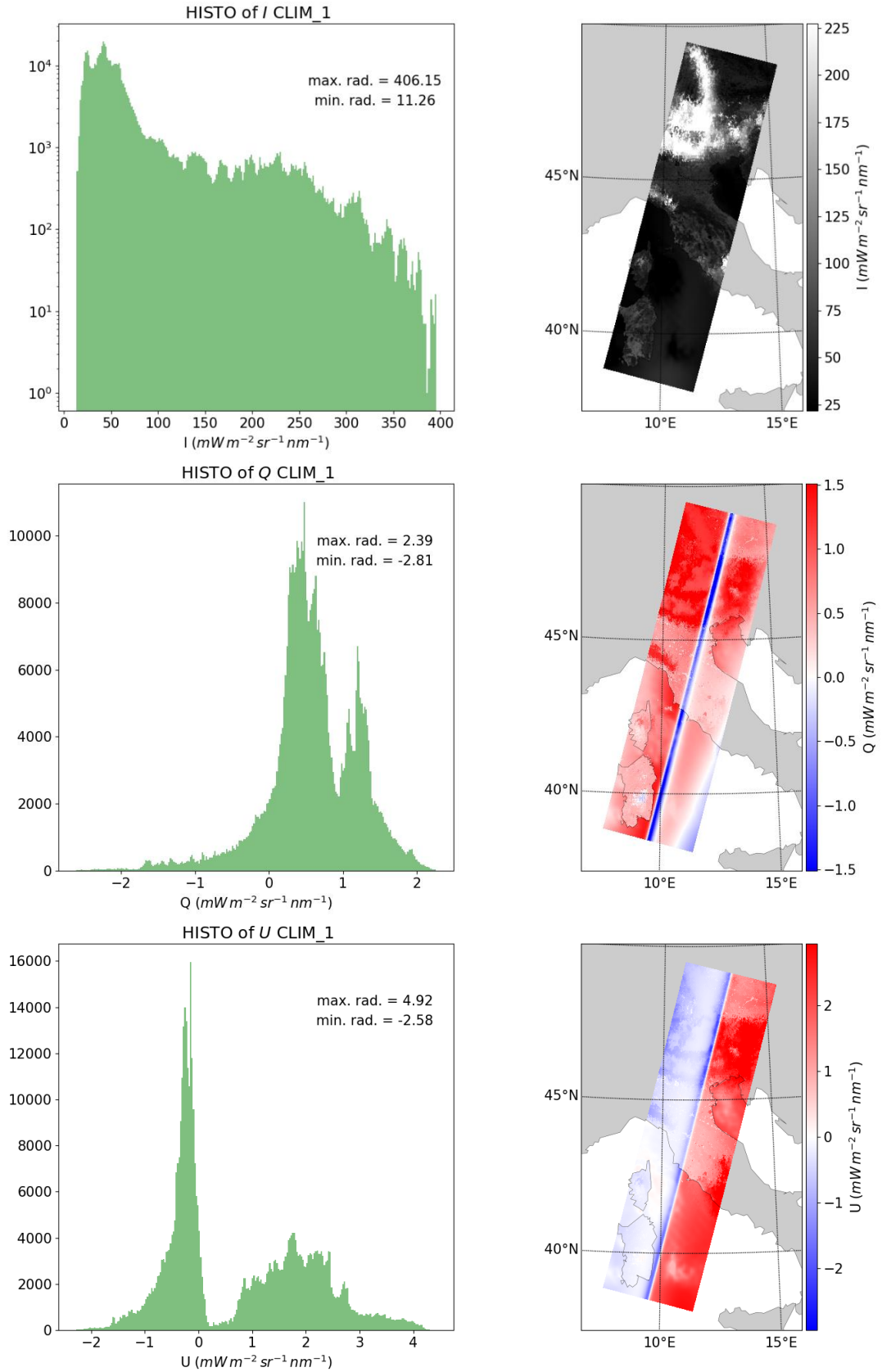

Figure 31 Radiance, and corresponding histogram, computed for granule S7A_CLI_1B_RAD_____N_20250703T111539_20250703T111839 (part of EUcent Nadir mode orbit) for CLIM channel 1 (670 nm). Upper panel, middle panel and lower panel show I, Q and U Stokes parameters respectively.

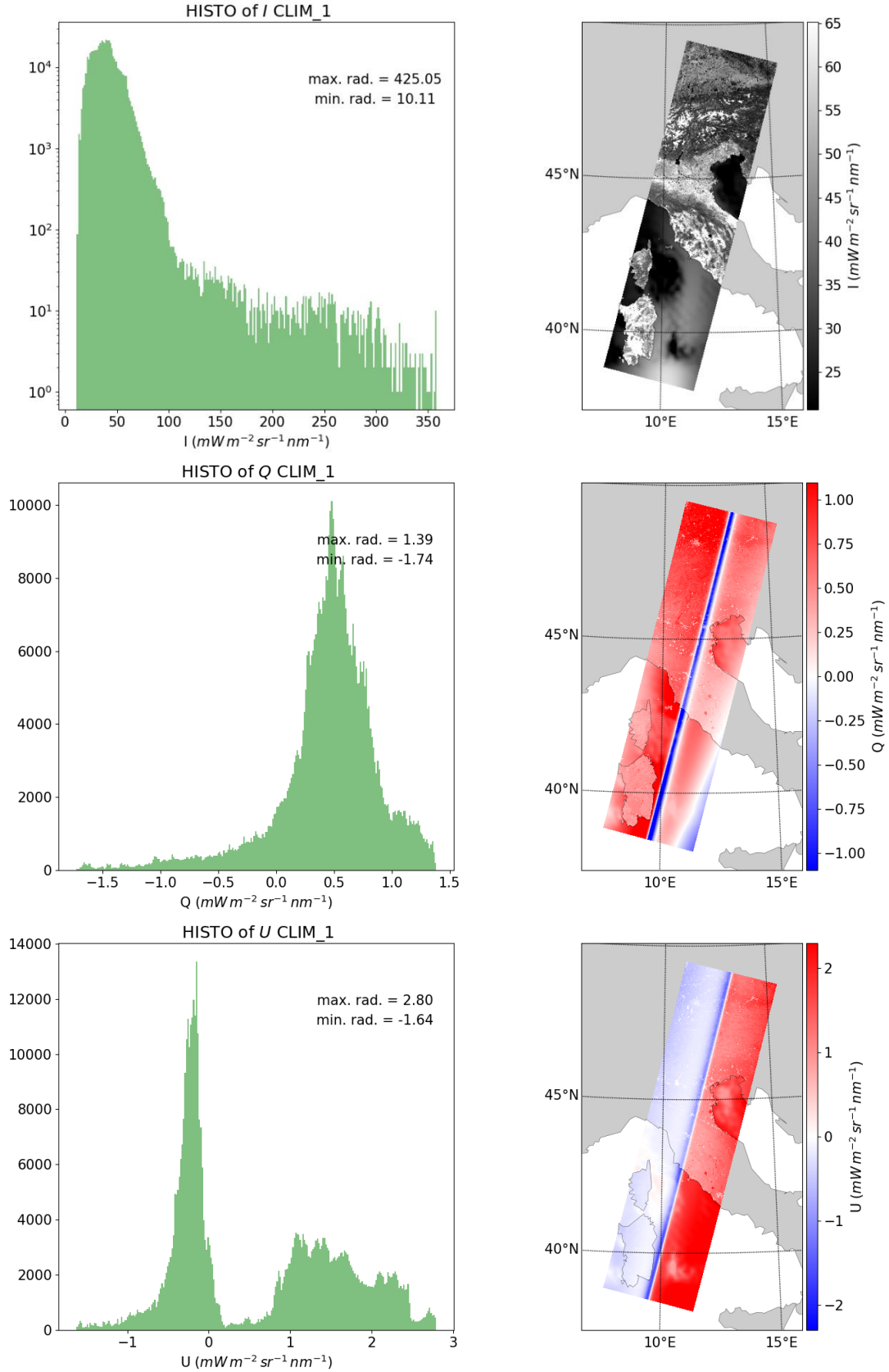

Figure 32 Radiance, and corresponding histogram, computed for granule S7A_CLI_1B_RAD_____N_20250703T111539_20250703T111839 (part of EUcent Nadir mode orbit) for CLIM channel 1 (670 nm) assuming full clear sky situation. Upper panel, middle panel and lower panel show I, Q and U Stokes parameters respectively.

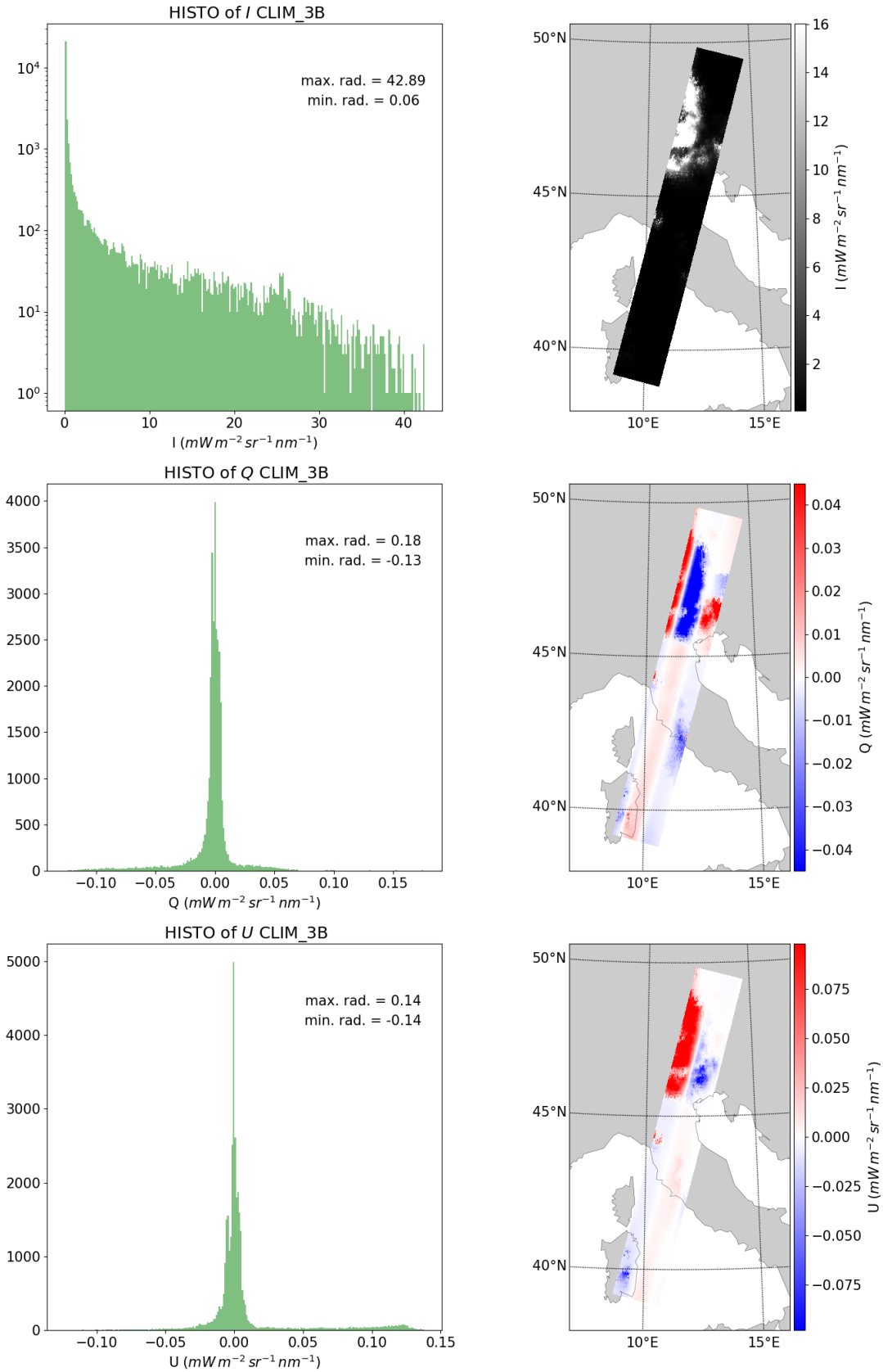

Figure 33 Radiance, and corresponding histogram, computed for granule S7A_CLI_1B_RAD_____N_20250703T111539_20250703T111839 (part of EUcent Nadir mode orbit) for CLIM channel 3B (1370 nm). Upper panel, middle panel and lower panel show I, Q and U Stokes parameters respectively.

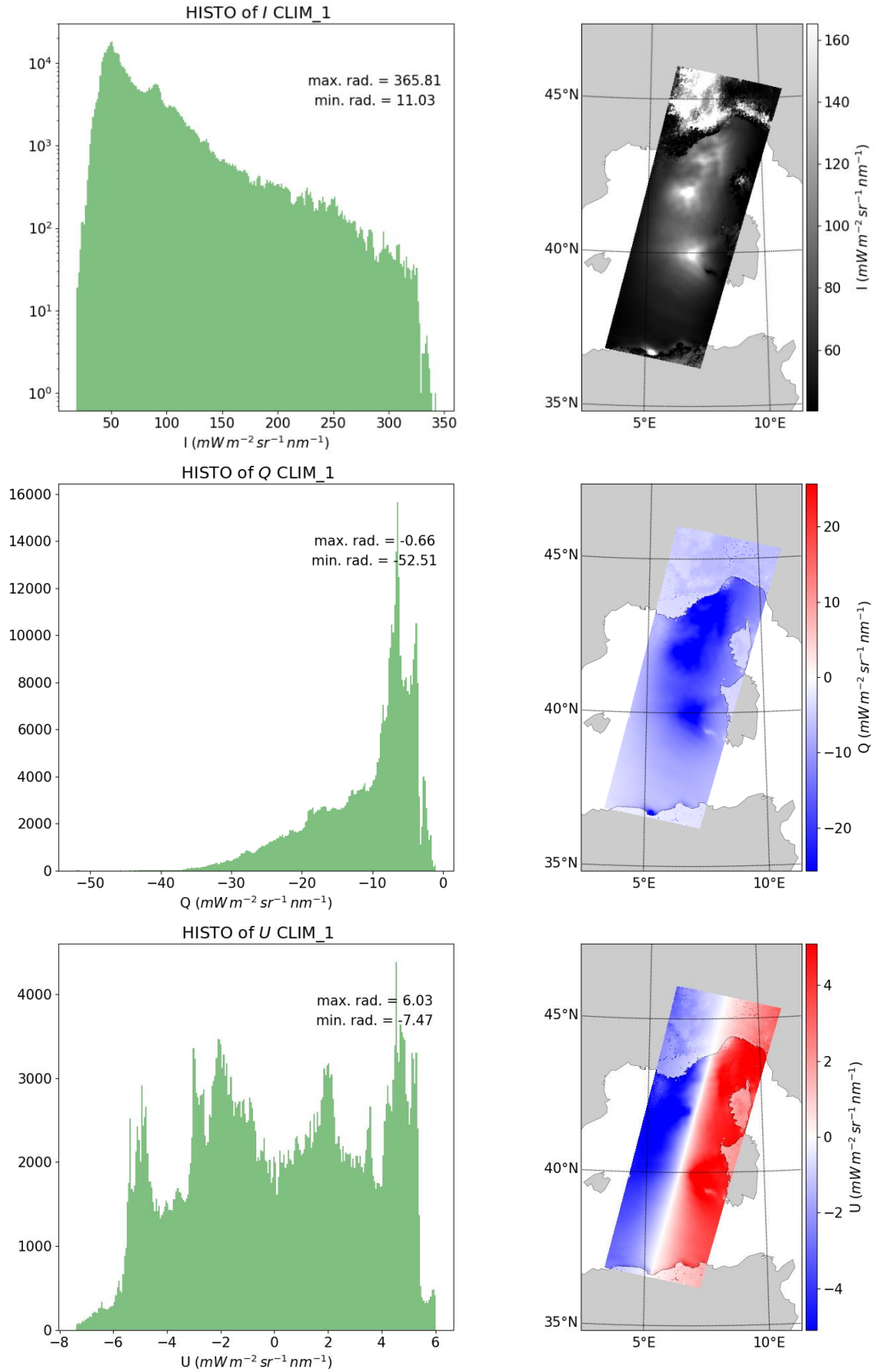

Figure 34 Radiance, and corresponding histogram, computed for granule S7A_CLI_1B_RAD_____OP_20250703T113347_20250703T113647 (part of EUwest pitched mode orbit) for CLIM channel 1 (670 nm). Upper panel, middle panel and lower panel show I, Q and U Stokes parameters respectively.

12. MAP L1C test data

12.1. L1C format and test data production

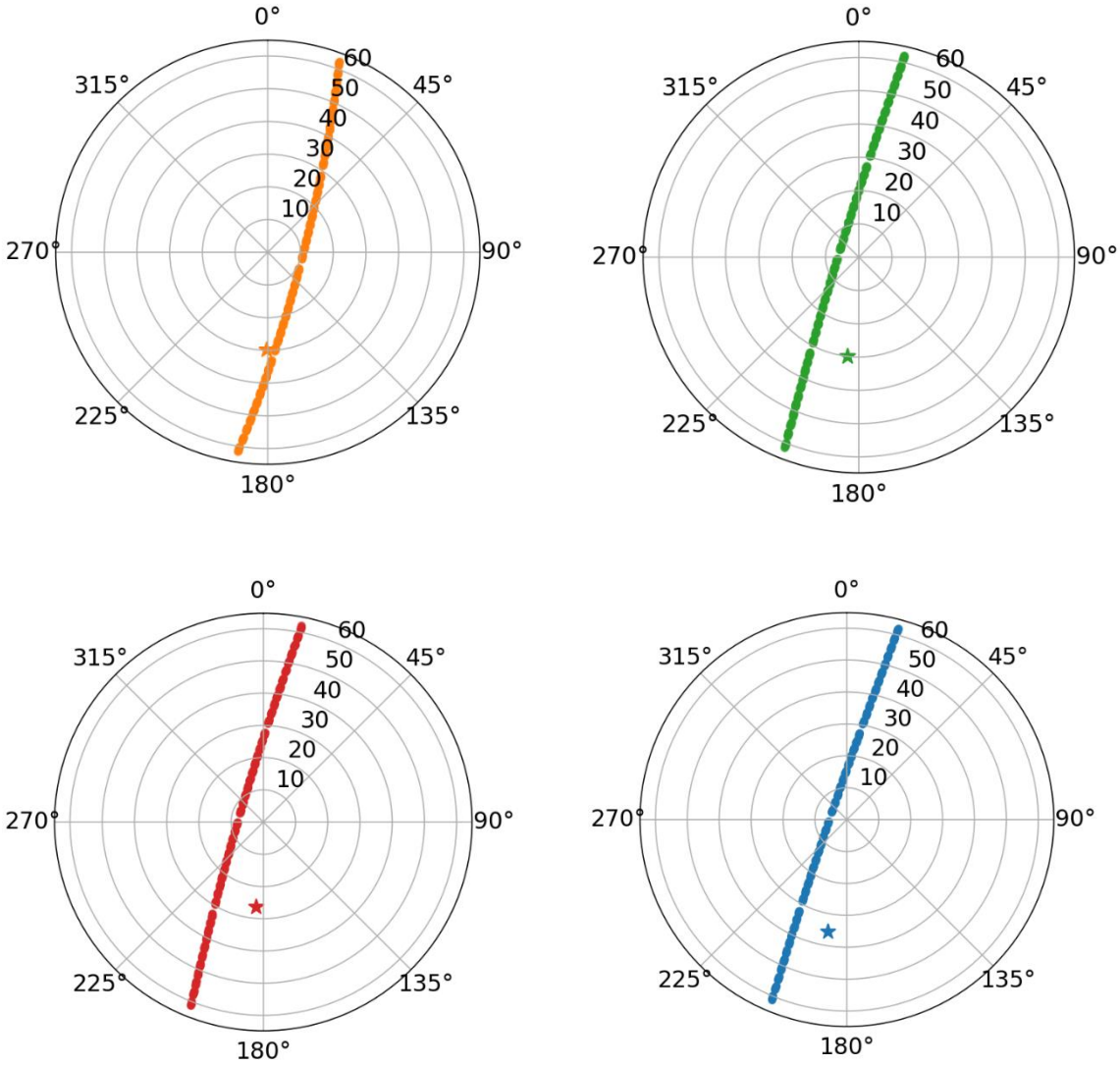

Figure 35 Polar plot for observing (viewing) geometries of 4 different pixels of MAP L1C granule S7A_MAP_1C_RAD_____ON_20250703T111239_20250703T111539 ("Berlin" granule, part of EUcent orbit). The locations of these 4 pixels are shown on Figure 36 (same colour code for points). The solar geometry is represented by the star.

The MAP L1C results of collocating all L1B geometries of all cameras to a common latitude / longitude grid. One L1C file is obtained for each granule. The pixel footprint is larger than the L1B. For a granule, we have 621 x 110 pixels (along x across track) x 45 geometries.

We produced test data (including clouds and assuming full clear sky situation) for which the scenario files were directly produced in the L1C grid and the radiative transfer solved for each geometry in that grid. This corresponds to a case where the 45 geometries and all wavelengths would perfectly be collocated. The production concerns the 6 orbits as for L1B test data. The scenario is built in the same way as for the L1B case. As for L1B files, the computed radiances are written in the L1C files provided by EUMETSAT.

Figure 35 shows polar plot for observing (viewing) geometries of 4 different pixels of MAP L1C granule S7A_MAP_1C_RAD_____ON_20250703T111239_20250703T111539 (“Berlin” granule, part of EUcent orbit). The locations of these 4 pixels are shown on Figure 36 (same colour code for points). The solar geometry is represented by the star. It varies only slightly over the 45 geometries and the mean is shown here for clarity. Azimuth angles are in local topocentric frame of the Sun / satellite direction, measured from the local north and positive towards the East on the Earth surface. Zenith angles are between local zenith direction and Sun / satellite direction on the Earth surface.

12.2. Resulting radiance

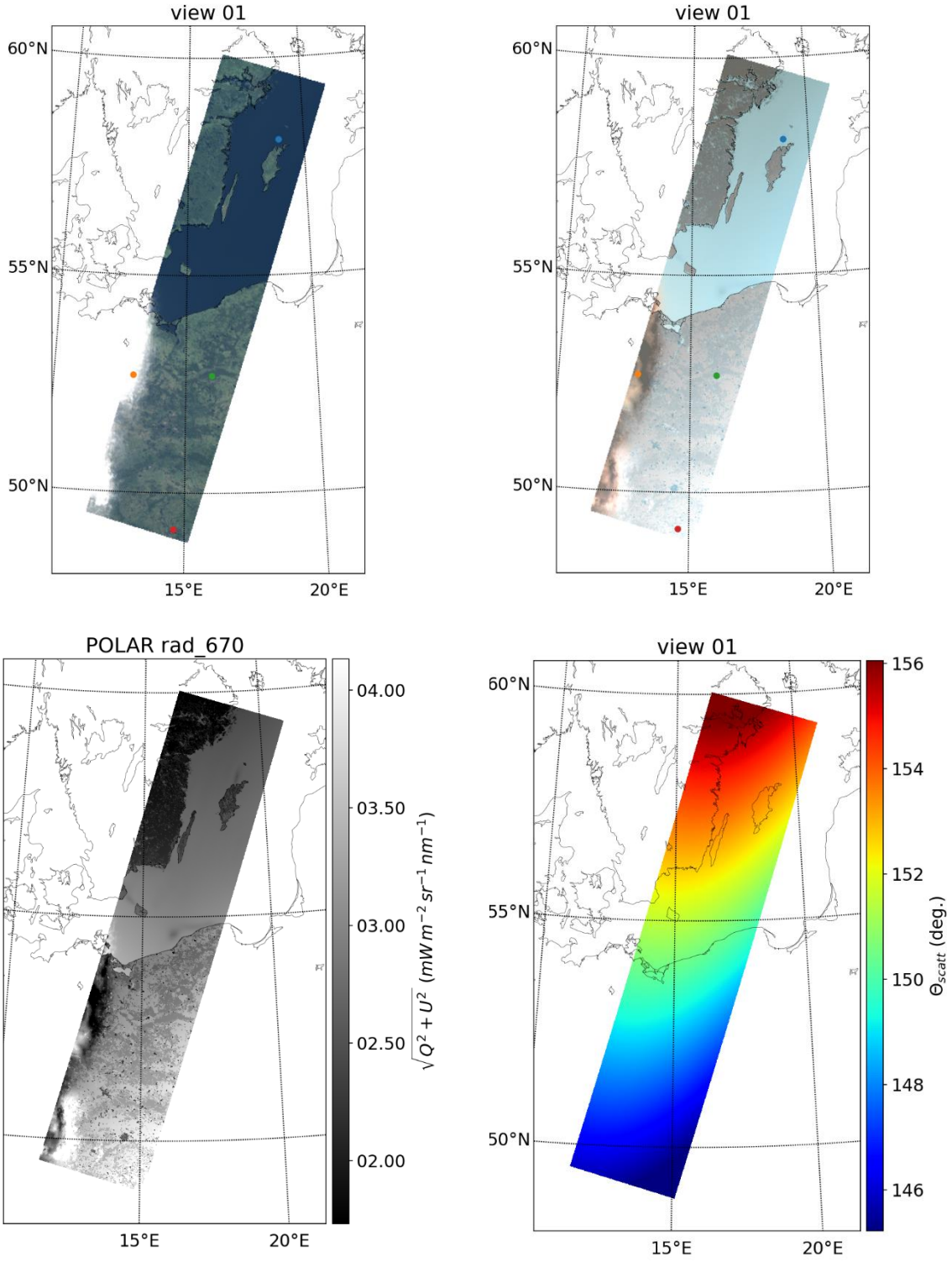

Figure 36 RGB (670 nm, 555 nm, 490 nm) view of MAP L1C granule S7A_MAP_1C_RAD_____ON_20250703T111239_20250703T111539 ("Berlin" granule, part of EUcent orbit) for geometry 1. Upper left panel shows the total radiance while the upper right panel shows the polarized radiance ($\sqrt{Q^2+U^2}$). Also shown are the polarized radiance ($\sqrt{Q^2+U^2}$) at 670 nm only (lower left panel) and the scattering angle (lower right panel).

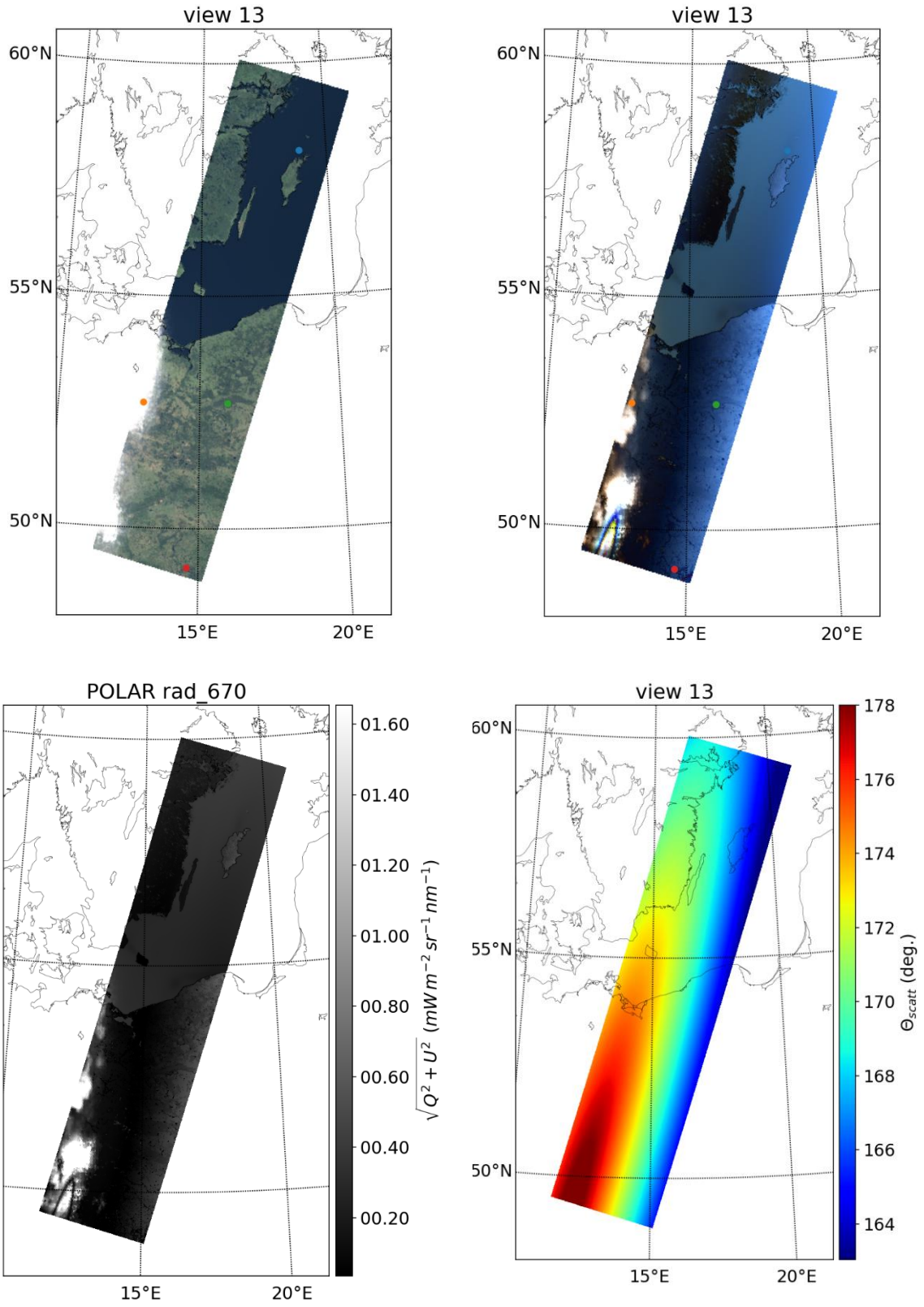

Figure 37 RGB (670 nm, 555 nm, 490 nm) view of MAP L1C granule S7A_MAP_1C_RAD_____ON_20250703T111239_20250703T111539 ("Berlin" granule, part of EUcent orbit) for geometry 13. Upper left panel shows the total radiance while the upper right panel shows the polarized radiance ($\sqrt{Q^2+U^2}$). Also shown are the polarized radiance ($\sqrt{Q^2+U^2}$) at 670 nm only (lower left panel) and the scattering angle (lower right panel).

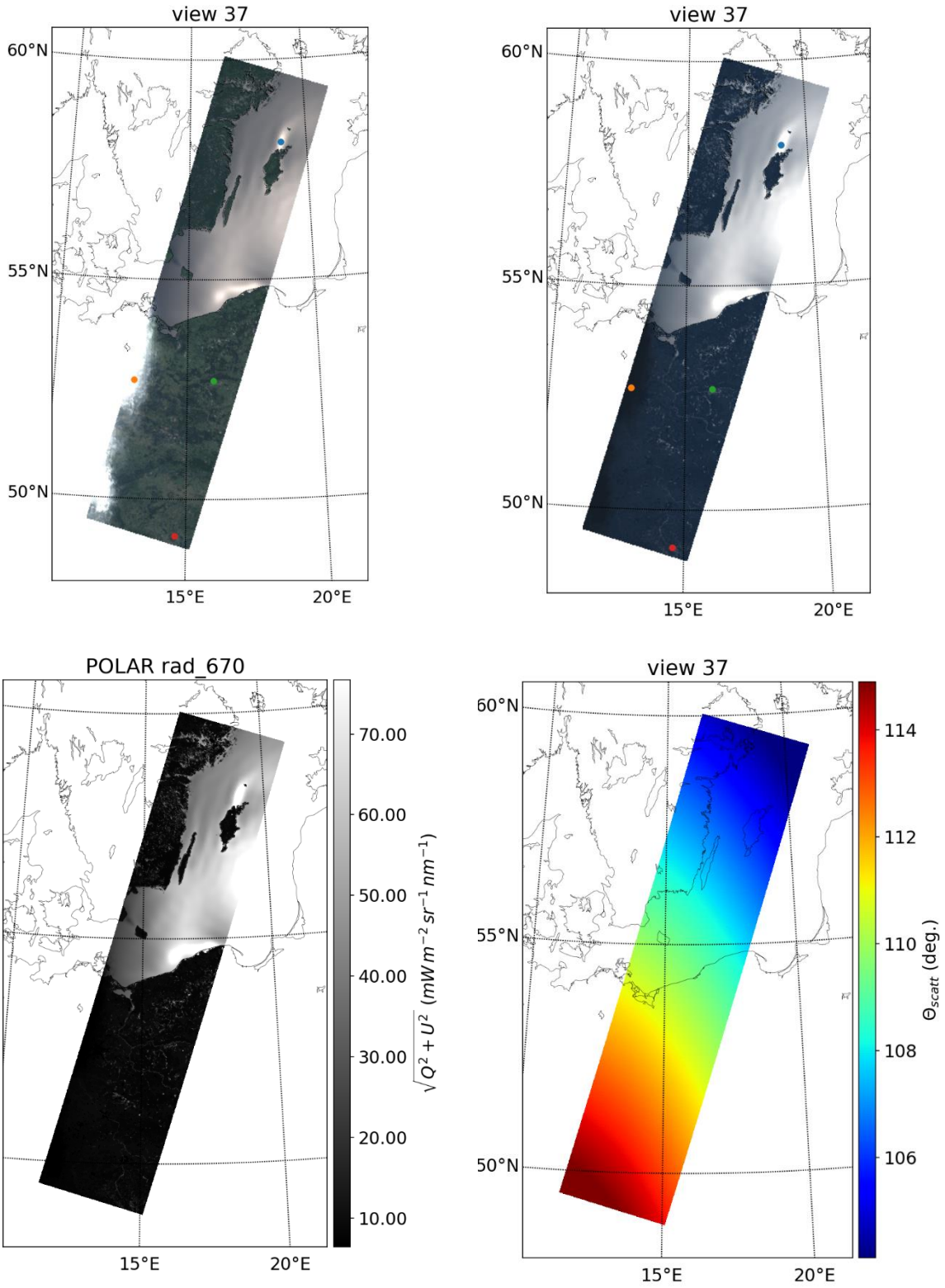

Figure 38 RGB (670 nm, 555 nm, 490 nm) view of MAP L1C granule S7A_MAP_1C_RAD_____ON_20250703T111239_20250703T111539 ("Berlin" granule, part of EUcent orbit) for geometry 37. Upper left panel shows the total radiance while the upper right panel shows the polarized radiance ($\sqrt{Q^2+U^2}$). Also shown are the polarized radiance ($\sqrt{Q^2+U^2}$) at 670 nm only (lower left panel) and the scattering angle (lower right panel).

Figure 36, Figure 37 and Figure 38 show RGB (670 nm, 555 nm, 490 nm) representation of MAP L1C granule S7A_MAP_1C_RAD_____ON_20250703T111239_20250703T111539 ("Berlin" granule, part of EUcent orbit) for geometry 1, 13 and 37 respectively. Upper left panel shows the total radiance while the lower right panel shows the polarized radiance ($\sqrt{Q^2 + U^2}$). It also shows the polarized radiance ($\sqrt{\mathrm{Q}^2 + \mathrm{U}^2}$) at 670 nm only (lower left panel) and the scattering angle (lower right panel). On geometry 1, we clearly see the depolarization caused by ice cloud on the South-West of the image. Liquid cloud polarized radiance appears white while over the sea we see a blue tint due to the polarization being dominated by the Rayleigh scattering. Geometry 13 is interesting because we see the glory in the South-West of the image, cause by near back scattering over liquid cloud. Finally, the geometry 37 shows a strong glitter dominating the polarization. We see the variability of wind speed impacting the structure of the glitter.

13. List of acronyms

ARTDECO	Atmospheric Radiative Transfer Database for Earth Climate Observation
BPDF	Bidirectionnal Polarization Distribution Function
BRDF	Bidirectionnal Reflectance Distribution Function
CAMS	Copernicus Atmosphere Monitoring Service
CCI	Climate Change Initiative
CHE	CO2 Human Emissions Project
CLIM	Cloud Imager
CO2M	Copernicus CO2 Monitoring Mission
COT	Cloud Optical Thickness
CPU	Central processing Unit
DEM	Digital Elevation Model
FWHM	Full Width at Half the Maximum
IGBP	International Geosphere Biosphere Programme
IWC	Ice Water Content
LSM	Land Sea Mask
LUT	Look-Up Table
LWC	Liquid Water Content
MAP	Multi-Angle Polarimeter
NDVI	Normalised Difference Vegetation Index
OZA	Observation Zenith Angle
PCA	Principal Component Analysis
RAL	Rutherford Appelton Laboratory
RTE	Radiative Transfer Equation
RTM	Radiative Transfer Model
SIF	Sun Induced Fluorescence
SRDS	Satellite Radiance Data Simulator
SRF	Spectral Response Function
SSRD	Space Segment Requirement Document
SZA	Sun Zenith Angle
TOA	Top Of Atmosphere
WSA	White Sky Albedo

14. References

Baum, B. A., Yang, P., Heymsfield, A. J., Bansemer, A., Cole, B. H., Merrelli, A., . . . Wang, C. (2014, 10). Ice cloud single-scattering property models with the full phase matrix at wavelengths from 0.2 to 100 µm. *\jqsrt, 146*, 123-139. doi:10.1016/j.jqsrt.2014.02.029

Bodhaine, B. A., Wood, N. B., Dutton, E. G., & Slusser, J. R. (1999, 11). On Rayleigh Optical Depth Calculations. *Journal of Atmospheric and Oceanic Technology, 16*, 1854. doi:10.1175/1520-0426(1999)016<1854:ORODC>2.0.CO;2

Buras, R., Dowling, T., & Emde, C. (2011, 8). New secondary-scattering correction in DISORT with increased efficiency for forward scattering. *\jqsrt, 112*, 2028-2034.

Clough, S. A., Shephard, M. W., Mlawer, E. J., Delamere, J. S., Iacono, M. J., Cady-Pereira, K., . . . Brown, P. D. (2005). Atmospheric radiative transfer modeling: a summary of the AER codes. *Journal of Quantitative Spectroscopy and Radiative Transfer, 91*, 233-244. doi:https://doi.org/10.1016/j.jqsrt.2004.05.058

de Haan, J. F., Bosma, P. B., & Hovenier, J. W. (1987, 9). The adding method for multiple scattering calculations of polarized light. *A&A, 183*, 371-391.

de Rooij, W. A. (1985). Reflection and transmission of polarized light by planetary atmospheres.

Devi, V. M., Benner, D. C., Brown, L. R., Miller, C. E., & Toth, R. A. (2007). Line mixing and speed dependence in CO2 at 6227.9cm−1: Constrained multispectrum analysis of intensities and line shapes in the 30013←00001 band. *Journal of Molecular Spectroscopy, 245*, 52-80. doi:https://doi.org/10.1016/j.jms.2007.05.015

Edwards, D. P., & Francis, G. L. (2000, 7). Improvements to the correlated-k radiative transfer method: Application to satellite infrared sounding. *\jgr, 105*, 18. doi:10.1029/2000JD900131

Evans, K. F., Walter, S. J., Heymsfield, A. J., & Deeter, M. N. (1998). Modeling of Submillimeter Passive Remote Sensing of Cirrus Clouds. *Journal of Applied Meteorology, 37*, 184-205. doi:10.1175/1520-0450(1998)037<0184:MOSPRS>2.0.CO;2

Hermans, C., Vandaele, A. C., & Fally, S. (2009). Fourier Transform measurements of $\mathrm{SO_2}$ absorption cross sections: I. Temperature dependence in the $23500 - 29000\;\mathrm{cm^{-1}}$ (345-425~nm) region. *Journal of Quantitative Spectroscopy and Radiative Transfer, 110*, 756-765. doi:10.1016/j.jqsrt.2009.01.031

Hogan, R. J., & Matricardi, M. (2020). Evaluating and improving the treatment of gases in radiation schemes: the Correlated K-Distribution Model Intercomparison Project (CKDMIP). *Geoscientific Model Development, 13*, 6501–6521. doi:10.5194/gmd-13-6501-2020

Kochanov, R. V., Gordon, I. E., Rothman, L. S., Shine, K. P., Sharpe, S. W., Johnson, T. J., . . . Hill, C. (2019). Infrared absorption cross-sections in HITRAN2016 and beyond: Expansion for climate, environment, and atmospheric applications. *Journal of Quantitative Spectroscopy and Radiative Transfer*. doi:10.1016/j.jqsrt.2019.04.001

Kokhanovsky, A. A., Budak, V. P., Cornet, C., Duan, M., Emde, C., Katsev, I. L., . . . Mayer, B. (2010). Benchmark results in vector atmospheric radiative transfer. *Journal of Quantitative Spectroscopy and Radiative Transfer, 111*, 1931–1946. Retrieved from http://linkinghub.elsevier.com/retrieve/pii/S0022407310000919

Kotchenova, S. Y., & Vermote, E. F. (2007, 7). Validation of a vector version of the 6S radiative transfer code for atmospheric correction of satellite data. Part II. Homogeneous Lambertian and anisotropic surfaces. *ao, 46*, 4455-4464. doi:10.1364/AO.46.004455

Kurucz, R. (1992). Synthetic infrared spectra. *Proceedings of the 154thSymposium of the International Astronomical Union (IAU)*.

Lacis, A. A., & Oinas, V. (1991, 5). A description of the correlated-k distribution method for modelling nongray gaseous absorption, thermal emission, and multiple scattering in vertically inhomogeneous atmospheres. *jgr, 96*, 9027-9064. doi:10.1029/90JD01945

Lamouroux, J., Régalia, L., Thomas, X., Auwera, J. V., Gamache, R. R., & Hartmann, J.-M. (2015). CO2 line-mixing database and software update and its tests in the 2.1µm and 4.3µm regions. *Journal of Quantitative Spectroscopy and Radiative Transfer, 151*, 88-96. doi:https://doi.org/10.1016/j.jqsrt.2014.09.017

Lucht, W., Schaaf, C. B., & Strahler, A. H. (2000, 3). An algorithm for the retrieval of albedo from space using semiempirical BRDF models. *IEEE Transactions on Geoscience and Remote Sensing, 38*, 977-998. doi:10.1109/36.841980

Maignan, F., Bréon, F.-M., & Lacaze, R. (2004). Bidirectional reflectance of Earth targets: Evaluation of analytical models using a large set of spaceborne measurements with emphasis on the Hot Spot. *Remote Sensing of Environment, 90*, 210-220. Retrieved from http://www.scopus.com/inward/record.url?eid=2-s2.0-1542349929&partnerID=40&md5=e7e3ad20e86ba9c400b634b1704d3c2d

Maignan, F., Breon, F.-M., Fedele, E., & Bouvier, M. (2009). Polarized reflectances of natural surfaces: Spaceborne measurements and analytical modeling. *Remote Sensing of Environment, 113*, 2642-2650. doi:10.1016/j.rse.2009.07.022

Meerdink, S. K., Hook, S. J., Roberts, D. A., & Abbott, E. A. (2019). The ECOSTRESS spectral library version 1.0. *Remote Sensing of Environment, 230*, 111196. doi:https://doi.org/10.1016/j.rse.2019.05.015

Mishchenko, M. I., & Travis, L. D. (1997). Satellite retrieval of aerosol properties over the ocean using polarization as well as intensity of reflected sunlight. *jgr, 102*, 16989-17014. doi:10.1029/96JD02425

Mlawer, E. J., Payne, V. H., Moncet, J.-L., Delamere, J. S., Alvarado, M. J., & Tobin, D. C. (2012). Development and recent evaluation of the MT_CKD model of continuum absorption. *Philosophical Transactions of the Royal Society of London A: Mathematical, Physical and Engineering Sciences, 370*, 2520–2556. doi:10.1098/rsta.2011.0295

Nakajima, T., & Tanaka, M. (1988, 7). Algorithms for radiative intensity calculations in moderately thick atmospheres using a truncation approximation. *jqsrt, 40*, 51-69. doi:10.1016/0022-4073(88)90031-3

RAL. (2021). *Provision of Top-Of-Atmospheresimulations for the evaluation ofdata processing for the CO2monitoring mission.* Tech. rep., RAL.

Reddy, M. S., Boucher, O., Bellouin, N., Schulz, M., Balkanski, Y., Dufresne, J.-L., & Pham, M. (2005). Estimates of global multicomponent aerosol optical depth and direct radiative perturbation in the Laboratoire de Météorologie Dynamique general circulation model. *Journal of Geophysical Research: Atmospheres, 110*. doi:10.1029/2004JD004757

Rothman, L. S., Gordon, I. E., Babikov, Y., Barbe, A., Benner, D. C., Bernath, P. F., . . . Wagner, G. (2013). The HITRAN2012 molecular spectroscopic database. *Journal of Quantitative Spectroscopy and Radiative Transfer, 130*, 4-50. doi:https://doi.org/10.1016/j.jqsrt.2013.07.002

Schreier, F., & García, S. G. (2013, 5). Py4CAtS - Python tools for line-by-line modelling of infrared atmospheric radiative transfer. *American Institute of Physics Conference Series*, *1531*, pp. 123-126. doi:10.1063/1.4804723

Vandaele, A. C., Hermans, C., Simon, P. C., Carleer, M., Colin, R., Fally, S., . . . Coquart, B. (1997). Measurements of the NO_2 absorption cross-section from 42000 cm-1 to 10000 cm-1 (238-1000 nm) at 220 K and 294 K. *Journal of Quantitative Spectroscopy and Radiative Transfer, 59*, 171-184. doi:10.1016/S0022-4073(97)00168-4

Wen, S., & Rose, W. I. (1994). Retrieval of sizes and total masses of particles in volcanic clouds using AVHRR bands 4 and 5. *Journal of Geophysical Research: Atmospheres, 99*, 5421-5431. doi:https://doi.org/10.1029/93JD03340

Wiscombe, W. J. (1977, 9). The Delta-M Method: Rapid Yet Accurate Radiative Flux Calculations for Strongly Asymmetric Phase Functions. *Journal of Atmospheric Sciences, 34*, 1408-1422. doi:10.1175/1520-0469(1977)034<1408:TDMRYA>2.0.CO;2